


Displacement field tunable superconductivity in an inversion-symmetric twisted van der Waals heterostructure

Harley D. Scammell¹ and Mathias S. Scheurer²

¹*School of Mathematical and Physical Sciences, University of Technology Sydney, Ultimo, NSW 2007, Australia*

²*Institute for Theoretical Physics III, University of Stuttgart, 70550 Stuttgart, Germany*

 (Received 29 August 2023; revised 10 January 2024; accepted 11 January 2024; published 25 January 2024)

We investigate the superconducting properties of inversion-symmetric twisted trilayer graphene by considering different parent states, including spin-singlet, triplet, and SO(4) degenerate states, with or without nodal points. By placing transition metal dichalcogenide layers above and below twisted trilayer graphene, spin-orbit coupling is induced in TTLG and, due to inversion symmetry, the spin-orbit coupling does not spin split the bands. The application of a displacement field (D_0) breaks the inversion symmetry and creates spin splitting. We analyze the evolution of the superconducting order parameters in response to the combined spin-orbit coupling and D_0 -induced spin splitting. Utilizing symmetry analysis combined with both a direct numerical evaluation and a complementary analytical study of the gap equation, we provide a comprehensive understanding of the influence of spin-orbit coupling and D_0 on superconductivity. These results contribute to a better understanding of the superconducting order in twisted trilayer graphene.

DOI: [10.1103/PhysRevB.109.035159](https://doi.org/10.1103/PhysRevB.109.035159)

I. INTRODUCTION

In recent years, graphene moiré superlattices with small twist angles (around 1° – 2°) [1,2] have been studied for their potential to host various quantum many-body phases [3–30]. However, graphene’s weak intrinsic spin-orbit coupling (SOC) [31,32] limits the phenomenology and, thus, the potential applications of moiré superlattices built exclusively from graphene layers. Enhancing SOC can unlock many additional opportunities such as stabilizing topological phases [33,34], affecting the competition between instabilities [35–42], and enabling spintronics applications [43–45]. Transition metal dichalcogenide (TMD) layers, e.g., WSe₂ or MoSe₂, can be used to induce SOC in graphene [46–48]; the form of the proximitized SOC terms is well established for both single-layer [49–54] and nontwisted multilayer [55–58] graphene. Notably, the resulting SOC terms induced by the TMD layer can be tuned based on the choice of TMD and the twist angle relative to graphene [50–54,57,58]. While some experiments, e.g., Refs. [18,25], have demonstrated the impact of TMD layers on the correlated physics of graphene moiré systems, the role of the proximitized TMD layer in the observed phases is not always clear; the effect of SOC on the correlated physics of graphene moiré systems thereby remains an open question.

Arguably, the role of SOC has not been elucidated due to the absence of a systematic approach to switch on/off or tune the strength of spin-orbit coupling. In a recent work [59], we proposed a method to achieve this. Meanwhile, in the present work, we provide a detailed analysis of the consequences for superconductivity. In particular, this work provides a detailed classification and understanding of the superconducting states of twisted trilayer graphene (TTLG) and their evolution under inversion-symmetric-proximitized SOC combined with an applied displacement field (D_0). The inversion-symmetry-preserving proximitization of SOC allows for spin splitting

of the electronic bands, including those comprising the superconducting states, to be directly switched on/off and tuned with applied displacement field [59]. In this way, the displacement field has a direct influence on the superconducting states, allowing to control the mixture of different pairing channels and drive superconducting phase transitions. To comprehensively identify the key features of the superconducting states, we employ three complementary approaches—(i) an unbiased symmetry analysis, (ii) numerically solving the mean-field gap equations, allowing for arbitrary admixtures and momentum dependencies, and (iii) a perturbative analytical study of the gap equations; all three perspectives yield consistent results and allow us to draw a detailed picture of the evolution of superconductivity in spin-orbit-coupled TTLG. Moreover, it was established in Ref. [59] that the Fermi surfaces of TTLG can exhibit a Möbius-like spin texture; in this work we show, analytically, why this Möbius-texture is inherited by the superconducting order.

The rest of this paper is organized as follows. Section II A establishes the continuum models and subsequent band structure for the van der Waals heterostructure system both with/without inversion-symmetry. Thereafter we focus on the inversion symmetric case. Section II B details the mean-field/gap equation for the various possible superconducting order parameters. Section III performs a symmetry analysis of the evolution of the mean-field superconducting order parameter under combined SOC— including Rashba and Ising— as well as D_0 . Section IV A performs direct numerical computations of the evolution of the eigenvalues/vectors; Sec. IV B examines the nature of the superconducting-to-superconducting phase transition observed in the numerics, while Sec. IV C provides analytic arguments to further elucidate key findings of our numerics. The results of the proceeding sections related to nodeless superconducting order. Section IV D provides an analysis of nodal pairing,

which is motivated by recent experiment [60,61]. Finally, a discussion and outlook can be found in Sec. V.

II. MODEL AND SYMMETRIES

A. Continuum model

We utilize a three-layer expansion of the continuum model for twisted-bilayer graphene [62–67] to capture the band structure of the system. In order to formulate the Hamiltonian, we define $a_{\mathbf{k};\rho,l,\eta,s,\mathbf{G}}$ as the annihilation operator for an electron in graphene layer $l = 1, 2, 3$, with momentum \mathbf{k} in the moiré Brillouin zone (MBZ), and in sublattice $\rho = A, B$, valley $\eta = \pm$, spin $s = \uparrow, \downarrow$, and reciprocal moiré lattice (RML) vector $\mathbf{G} = \sum_j n_j \mathbf{G}_j$, where $n_j \in \mathbb{Z}$. Throughout our work, we use the same notation for Pauli matrices and the corresponding quantum numbers, so that ρ_j, s_j , and η_j are the Pauli matrices for sublattice, spin, and valley space, respectively, with $j = 0, 1, 2, 3$. To reveal the mirror symmetry σ_h of the system, we switch to its eigenbasis [65] by introducing the field operators $b_{\mathbf{k};\rho,\ell,\eta,s,\mathbf{G}}$,

$$a_{\mathbf{k};\rho,l,\eta,s,\mathbf{G}} = V_{l,\ell} b_{\mathbf{k};\rho,\ell,\eta,s,\mathbf{G}}, \quad V = \frac{1}{\sqrt{2}} \begin{pmatrix} 1 & 0 & -1 \\ 0 & \sqrt{2} & 0 \\ 1 & 0 & 1 \end{pmatrix}, \quad (1)$$

with $\ell = 1, 2$ ($\ell = 3$) corresponding to the mirror-even (mirror-odd) subspaces.

The continuum Hamiltonian is divided into four distinct parts, denoted as $h_{\mathbf{k},\eta} = h_{\mathbf{k},\eta}^{(g)} + h_{\mathbf{k},\eta}^{(t)} + h_{\mathbf{k}}^{(D)} + h_{\mathbf{k},\eta}^{(\text{SOC})}$. These correspond to the contribution of each individual graphene layer, the tunneling between the layers, the coupling to the electric displacement field, and the SOC terms induced by proximity. The TTLG contribution $h_{\mathbf{k},\eta}^{(g)} + h_{\mathbf{k},\eta}^{(t)}$ separates into an effective TBG, mirror-even $\ell = 1, 2$ subspace (denoted $h_{\mathbf{k},\eta}^{(\text{TBG})}$) and graphene, mirror-odd $\ell = 3$ subspace (denoted $h_{\mathbf{k},\eta}^{(\text{G})}$), such that

$$\begin{pmatrix} h_{\mathbf{k},\eta}^{(g)} + h_{\mathbf{k},\eta}^{(t)} \\ \rho,\ell,s,\mathbf{G};\rho',\ell',s',\mathbf{G}' \end{pmatrix} = \begin{pmatrix} & 0 \\ \left(h_{\mathbf{k},\eta}^{(\text{TBG})} \right)_{\rho,s,\mathbf{G};\rho',s',\mathbf{G}'} & 0 \\ 0 & 0 \end{pmatrix} \Big| \begin{pmatrix} h_{\mathbf{k},\eta}^{(\text{G})} \\ \rho,s,\mathbf{G};\rho',s',\mathbf{G}' \end{pmatrix}_{\ell,\ell'}. \quad (2)$$

The explicit forms of $h_{\mathbf{k},\eta}^{(g)}$ and $h_{\mathbf{k},\eta}^{(t)}$ (or equivalently $h_{\mathbf{k},\eta}^{(\text{TBG})}$ and $h_{\mathbf{k},\eta}^{(\text{G})}$) are presented in Appendix A. The displacement field mixes the mirror-even and odd subspaces,

$$\left(h_{\mathbf{k}}^{(D)} \right)_{\rho,\ell,s,\mathbf{G};\rho',\ell',s',\mathbf{G}'} = -D_0 \delta_{\rho,\rho'} \delta_{s,s'} \delta_{\mathbf{G},\mathbf{G}'} \begin{pmatrix} 0 & 0 & 1 \\ 0 & 0 & 0 \\ 1 & 0 & 0 \end{pmatrix}_{\ell,\ell'}, \quad (3)$$

as do the antisymmetric terms of SOC,

$$\left(h_{\mathbf{k},\eta}^{(\text{SOC})} \right)_{\rho,\ell,s,\mathbf{G};\rho',\ell',s',\mathbf{G}'} = \delta_{\mathbf{G},\mathbf{G}'} \begin{pmatrix} \left(h_{\eta}^s \right)_{\rho,s;\rho',s'} & 0 & \left(h_{\eta}^a \right)_{\rho,s;\rho',s'} \\ 0 & 0 & 0 \\ \left(h_{\eta}^a \right)_{\rho,s;\rho',s'} & 0 & \left(h_{\eta}^s \right)_{\rho,s;\rho',s'} \end{pmatrix}_{\ell,\ell'}, \quad (4)$$

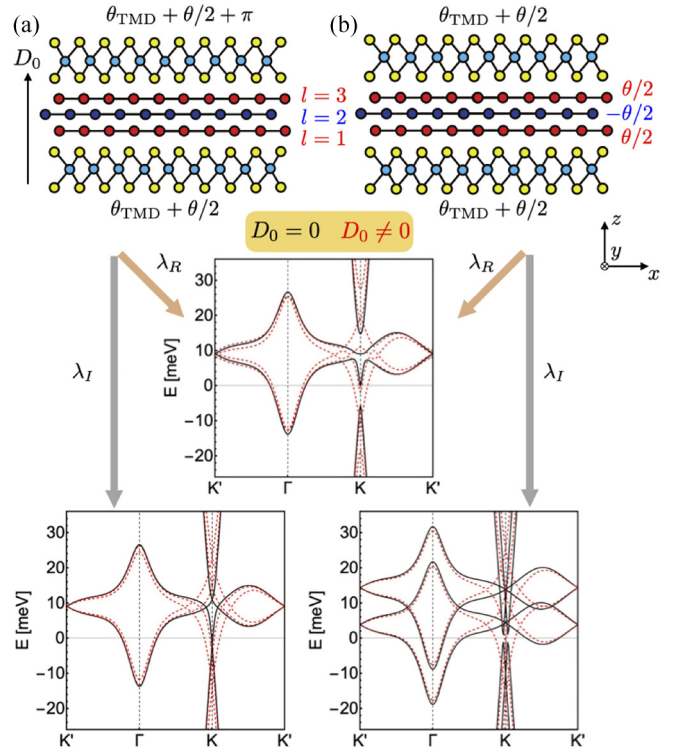


FIG. 1. Two distinct classes of configurations for the TMD/TTLG/TMD heterostructure and their representative band structures. (a) Inversion symmetric heterostructure (at $D_0 = 0$), whereby the upper TMD layer is antiparallel to the lower layer, and (b) mirror symmetric heterostructure (at $D_0 = 0$) with the TMD layers parallel. (Middle) Band structure for both configurations for $\{\lambda_R, \lambda_I\} = \{10, 0\}$ meV and $D_0 = 0$ ($D_0 = 30$) meV in black (dashed red); band structure is identical for both configurations as long as $\lambda_I = 0$. (Bottom left and right) Band structure for, respectively, the (a) and (b) configurations with $\{\lambda_R, \lambda_I\} = \{0, 10\}$ meV and $D_0 = 0$ ($D_0 = 30$) meV in black (dashed red).

i.e., the terms $(h_{\eta}^a)_{\rho,s;\rho',s'}$. The explicit form of $h^{(\text{SOC})}$ depends on the configuration of the TMD layers; we consider the two distinct configurations shown in Fig. 1, which correspond to (i) inversion symmetric and (ii) mirror symmetric. Explicitly, the setup (ii) is obtained from (i) by rotating the upper TMD layer by C_{2z} . We consider only “Rashba”- and “Ising”-type SOC, with couplings λ_R and λ_I , since these are known to be more dominant than any other type [50–54]. It is noteworthy that the relative strength of λ_R and λ_I can be tuned with the twist angle θ_{TMD} between the graphene and the TMD layers [50–54,57,58]. Upon transforming to the mirror eigenbasis, the h_{η}^s and h_{η}^a contributions for the setups (i) and (ii) are found to be

$$\begin{aligned} \text{(i): } & h_{\eta}^s = 0, \quad h_{\eta}^a = -\lambda_I s_z \eta - \lambda_R (\eta \rho_x s_y - \rho_y s_x), \\ \text{(ii): } & \tilde{h}_{\eta}^s = -\lambda_I s_z \eta, \quad \tilde{h}_{\eta}^a = -\lambda_R (\eta \rho_x s_y - \rho_y s_x). \end{aligned} \quad (5)$$

Both the Rashba and Ising terms are odd under C_{2z} and, since inversion $I = \sigma_{\eta} C_{2z}$, the h_{η}^a (h_{η}^s) are even (odd) under inversion, cf. Table I. Spin-splitting occurs when inversion symmetry is broken; for setup (i) having that $\tilde{h}_{\eta}^s = 0$ means that inversion symmetry is intact and there is no spin splitting

TABLE I. Action of the point symmetries of the continuum theory on the microscopic operators ψ_k in the continuum model, see Sec. II A, and the low-energy fermions c_k used, e.g., in Eqs. (7) and (12). For convenience of the reader, we also list redundant symmetries. In the last two columns, we state the constraints on D_0 , λ_R , and λ_I for the respective symmetry to be present for (i) the inversion and (ii) the mirror symmetric geometry, see Eq. (5) and Fig. 1.

Symmetry S	unitary?	$S\psi_{k;\ell}G S^\dagger$	$S c_k S^\dagger$	condition for (i)	condition for (ii)
$SO(3)_s$	✓	$e^{i\varphi_s/2}\psi_{k;\ell}G$	$e^{i\varphi_s/2}c_k$	$\lambda_R = \lambda_I = 0$	$\lambda_R = \lambda_I = 0$
$SO(2)_s$	✓	$e^{i\varphi_{sz}/2}\psi_{k;\ell}G$	$e^{i\varphi_{sz}/2}c_k$	$\lambda_R = 0$	$\lambda_R = 0$
C_{3z}	✓	$e^{i\frac{2\pi}{3}\rho_z}\psi_{C_{3z}k;\ell,C_{3z}G}$	$c_{C_{3z}k}$	$\lambda_R = 0$	$\lambda_R = 0$
C_{3z}^s	✓	$e^{i\frac{2\pi}{3}(\rho_z\eta_z+s_z)}\psi_{C_{3z}k;\ell,C_{3z}G}$	$e^{i\frac{2\pi}{3}s_z}c_{C_{3z}k}$	–	–
C_{2z}	✓	$\eta_x\rho_x\psi_{-k;\ell,-G}$	$\eta_x c_{-k}$	$\lambda_R = \lambda_I = 0$	$\lambda_R = \lambda_I = 0$
C_{2z}^s	✓	$s_z\eta_x\rho_x\psi_{-k;\ell,-G}$	$s_z\eta_x c_{-k}$	$\lambda_I = 0$	$\lambda_I = 0$
$C_{2z}^s = C_{2z}^s i s_{y,x}$	✓	$s_{x,y}\eta_x\rho_x\psi_{-k;\ell,-G}$	$s_{x,y}\eta_x c_{-k}$	$\lambda_R = 0$	$\lambda_R = 0$
σ_h	✓	$(1, 1, -1)_\ell\psi_{k;\ell}G$	$\pm c_k$	$D_0 = \lambda_R = \lambda_I = 0$	$D_0 = \lambda_R = 0$
σ_h^s	✓	$s_z(1, 1, -1)_\ell\psi_{k;\ell}G$	$\pm s_z c_k$	$D_0 = \lambda_I = 0$	$D_0 = 0$
$\sigma_h^s = \sigma_h^s i s_{y,x}$	✓	$s_{x,y}(1, 1, -1)_\ell\psi_{k;\ell}G$	$\pm s_{x,y} c_k$	$D_0 = \lambda_R = 0$	$D_0 = \lambda_R = \lambda_I = 0$
$I = C_{2z}\sigma_h = C_{2z}^s\sigma_h^s$	✓	$\eta_x\rho_x(1, 1, -1)_\ell\psi_{-k;\ell}G$	$\pm\eta_x c_{-k}$	$D_0 = 0$	$D_0 = \lambda_I = 0$
Θ	✗	$\eta_x\psi_{-k;\ell,-G}$	$\eta_x c_{-k}$	$\lambda_R = \lambda_I = 0$	$\lambda_R = \lambda_I = 0$
Θ^s	✗	$i s_y\eta_x\psi_{-k;\ell,-G}$	$i s_y\eta_x c_{-k}$	–	–

unless $D_0 \neq 0$. On the other hand, for setup (ii) having $\tilde{h}_\eta^s \neq 0$ explicitly breaks inversion-symmetry and thereby allows for spin splitting of the bands even at $D_0 = 0$. Figure 1 provides a comparison of the band structures for the two configurations. In line with Eq. (5), we see that the two setups have identical spectrum as long as $\lambda_I = 0$.

The spin splitting of the bands under SOC and D_0 is captured via $\mathbf{g}_k \neq 0$ in the effective Hamiltonian,

$$h_{k,\eta}^{\text{eff}} = s_0 \xi_{\eta,k} + \eta \mathbf{g}_{\eta,k} \cdot \mathbf{s}, \quad (6)$$

for the bands of tTLG near the Fermi level, where ξ_k is the spin-independent part of the band structure. To be concrete, Fig. 2 presents the band structure, Fermi surfaces and spin texture for the case $\lambda_R, D_0 \neq 0$. As discussed in detail in Ref. [59], $\mathbf{g}_{\eta,k}$ exhibits vortices at three generic momenta inside the Brillouin zone which lead to three (almost) crossing points of the Fermi surface for a (close to a) specific value of the chemical potential. In Fig. 2(b), we tuned the system close to this point, which leads to the Möbius-like nature of the Bloch spin textures. In Sec. IV C we will use the notion of

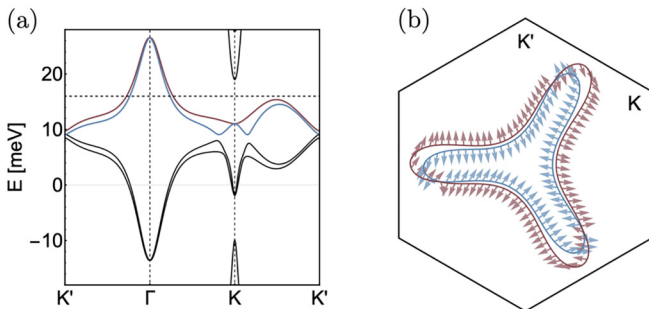


FIG. 2. (a) Band structure and (b) Fermi surfaces and their spin texture (arrows). Here twist angle $\theta = 1.75^\circ$, $\varepsilon_F = 16$ meV, $\lambda_R = 20$ meV, $\lambda_I = 0$, $D_0 = 10$ meV, and valley $\eta = +$.

the $\mathbf{g}_{\eta,k}$ vector to make analytic statements about the properties of the superconducting states.

B. Superconductivity

We present a minimal interacting model used to capture the various possibilities of superconductivity in TTLG, which we refer to as the *parent superconducting state*. For the parent superconducting state, we exclusively consider intervalley pairing, not intravalley pairing, which is expected to be dominant; this is due to the guarantee of a nesting logarithm through time-reversal symmetry. On top of this, we account for the possibilities [68–71] of spin-singlet dominant, spin-triplet dominant, and high-symmetry spin-SO(4) pairing, as well as both nodal and nodeless superconductivity—corresponding to the 1D and 2D IRs of C_{3z}^s , respectively. We assume that the Cooper pairs of the parent state are formed from the partially filled, spin-degenerate band, consistent with experimental observations [19,20,25,26].

Let $\varepsilon_{\eta,s,k}^0$ and $\psi_{\eta,s,k}^0$ denote the spin-degenerate bands and corresponding eigenfunctions at the Fermi level of the unperturbed system ($h_\eta^{(g)} + h_\eta^{(t)}$) with quantum numbers: spin s ; graphene valley η ; and quasimomenta \mathbf{k} restricted to the MBZ. We denote the corresponding creation operator $c_{k,\eta,s}^\dagger$. The combined perturbations of SOC and D_0 are captured in the perturbed eigenvectors of the noninteracting Hamiltonian, $h_{k,\eta}\psi_{\eta,n,k} = \varepsilon_{\eta,n,k}\psi_{\eta,n,k}$, with $h_\eta = h_\eta^{(g)} + h_\eta^{(t)} + h_\eta^{(\text{SOC})} + h_\eta^{(\text{D})}$. The band index n replaces spin s which is no longer a good quantum number. The electron creation operators for the Bloch states of the perturbed system, $\tilde{c}_{k,\eta,n}^\dagger$, are related to the unperturbed creation operators via

$$c_{k,\eta,s}^\dagger = \sum_n C_{\eta,n,s,k}^* \tilde{c}_{k,\eta,n}^\dagger, \quad C_{\eta,n,s,k}^* \equiv \langle \psi_{\eta,n,k} | \psi_{\eta,s,k}^0 \rangle. \quad (7)$$

The mean-field Hamiltonian, decoupled into the Cooper channel for intervalley pairing, is valley-diagonal $\mathcal{H} = \sum_{\eta=\pm} \mathcal{H}_\eta$

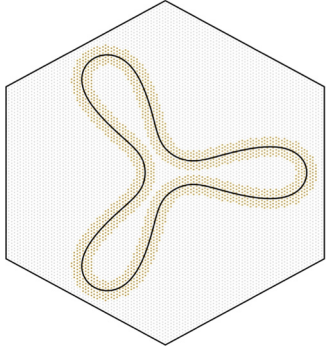


FIG. 3. The discrete grid realization of the $\Theta_{k;\varepsilon_F}$ -functions of Eq. (9); black curve is the Fermi surface of the unperturbed system at $\varepsilon_F = 9.5$ meV and $\theta = 1.50^\circ$, orange points indicate $\Theta_{k;\varepsilon_F} = 1$, gray points indicate $\Theta_{k;\varepsilon_F} = 0$.

with

$$\begin{aligned} \mathcal{H}_\eta = & \sum_{k,n} \varepsilon_{\eta,n,k} \tilde{c}_{k,\eta,n}^\dagger \tilde{c}_{k,\eta,n} \\ & + \sum_{k_1,k_2;\mu,\nu} (-\Gamma^{-1})_{k_1,k_2;\mu,\nu} (d_{k_1,\eta}^*)_\mu (d_{k_2,\eta})_\nu \\ & + \sum_k \sum_{n,n'} \sum_{s_1,s_2} \sum_\mu \{ \tilde{c}_{k,\eta,n}^\dagger \tilde{c}_{-k,\eta,n'}^\dagger \\ & \times [(d_{k,\eta})_\mu (s_\mu i s_y)_{s_1,s_2} C_{\eta,n,s_1,k}^* C_{\eta,n',s_2,k}] + \text{H.c.} \}. \quad (8) \end{aligned}$$

Here the intervalley superconducting order parameter $d_{\mu,k,\eta}$ encodes the spin, quasimomentum and valley structure, where $\mu = 0$ refers to spin singlet and $\mu = 1, 2, 3$ refer to the components of the spin triplet. We point out that the mean-field description of the *parent* superconducting state corresponds to the limit $C_{\eta,n,s,k} = 1$; for the *perturbed* superconducting state, the overlap factors $C_{\eta,n,s,k}$ encode the SOC-induced mixing of the μ components of $d_{\mu,k,\eta}$ as a function of \mathbf{k} . Here we allow the vertex $\Gamma_{k_1,k_2;\mu,\nu}$ to be either even or odd under: $\mathbf{k}_1 \rightarrow -\mathbf{k}_1$ or $\mathbf{k}_2 \rightarrow -\mathbf{k}_2$. The even (odd) vertex is introduced to accommodate nodeless (nodal) superconductivity. Explicitly, $\Gamma_{k_1,k_2;\mu,\nu} = \Gamma_{k_1,k_2;\mu,\nu}^{\text{even}}$ or $\Gamma_{k_1,k_2;\mu,\nu}^{\text{odd}}$, with

$$\begin{aligned} \Gamma_{k_1,k_2;\mu,\nu}^{\text{even}} &= (\gamma_0 \delta_{\mu,\nu} + \delta\gamma \delta_{\mu,0} \delta_{\nu,0}) F_{k_1,k_2} \Theta_{k_1;\varepsilon_F} \Theta_{k_2;\varepsilon_F}, \\ \Gamma_{k_1,k_2;\mu,\nu}^{\text{odd}} &= \Gamma_{k_1,k_2;\mu,\nu}^{\text{even}} \times (\mathcal{X}_{k_1} \mathcal{X}_{k_2} + \mathcal{Y}_{k_1} \mathcal{Y}_{k_2}). \quad (9) \end{aligned}$$

Here F_{k_1,k_2} is a momentum dependent function (detailed in the Appendix B) while $\Theta_{k;\varepsilon_F}$ is a step-function such that: $\Theta_{k;\varepsilon_F} = 1$ for \mathbf{k} within a radius Λ of any Fermi momentum \mathbf{k}_F , and $\Theta_{k;\varepsilon_F} = 0$ elsewhere. A representative plot of $\Theta_{k;\varepsilon_F}$ is shown in Fig. 3. An attractive interaction requires $\gamma_0 > 0$. Meanwhile, the singlet-triplet asymmetry parameter $|\delta\gamma|/\gamma_0 < 1$ distinguishes three cases of the parent superconducting state: (i) $\delta\gamma > 0$ favors spin-singlet, (ii) $\delta\gamma < 0$ favors spin triplet, and (iii) for $\delta\gamma = 0$, spin singlet and triplet are degenerate [spin SO(4)]. Finally, in Eq. (9), we have included the basis functions $\mathcal{X}_k, \mathcal{Y}_k$, which are MBZ-periodic functions transforming as k_x, k_y under C_{3z} , and are specifically taken

to be

$$\begin{aligned} \mathcal{X}_k &= \frac{2}{\sqrt{3}} \sin\left(\frac{\sqrt{3}}{2} a_\theta k_x\right) \cos\left(\frac{1}{2} a_\theta k_y\right), \\ \mathcal{Y}_k &= \frac{2}{3} \left(\cos\left(\frac{\sqrt{3}}{2} a_\theta k_x\right) \sin\left(\frac{1}{2} a_\theta k_y\right) + \sin(a_\theta k_y) \right), \quad (10) \end{aligned}$$

with a_θ the magnitude of the moiré lattice vector. The chosen combination of $\mathcal{X}_k, \mathcal{Y}_k$ in $\Gamma_{k_1,k_2;\mu,\nu}^{\text{odd}}$ [Eq. (9)] preserves C_{3z} .

Following (8), we arrive at the linearized gap equation,

$$\begin{aligned} (d_{k_1,\eta})_\mu &= \sum_{\nu,k_2} \Gamma_{\mu,\mu',k_1,k_2} \mathcal{W}_{\mu'\nu,k_2,\eta} (d_{k_2,\eta})_\nu, \\ \mathcal{W}_{\mu\nu,k,\eta} &= \sum_{n_1,n_2} \sum_{s_1,s_2,s_3,s_4} \frac{\tanh\left(\frac{\varepsilon_{\eta,n_1k}}{2T}\right) + \tanh\left(\frac{\varepsilon_{\eta,n_2k}}{2T}\right)}{2(\varepsilon_{\eta,n_1k} + \varepsilon_{\eta,n_2k})} (\sigma_\mu)_{s_2,s_3} \\ &\quad \times C_{\eta,n_1,s_1,k} C_{\eta,n_1s_2,k}^* C_{\eta,n_2,s_3,k} C_{\eta,n_2,s_4,k}^* (\sigma_\nu)_{s_4,s_1}. \quad (11) \end{aligned}$$

We note that the gap equation is diagonal in η , and hence for the numerical analysis presented in Sec. IV we specialize to $\eta = +1$. In fact, this uniquely determines the superconducting order parameter since its form in the other valley just follows from the Fermi Dirac constraint [see Eq. (13) below]. Further details about solving the gap equation are presented in Appendix B.

III. SYMMETRY ANALYSIS

Before solving numerically for superconductivity in the next section, we here use symmetry arguments to derive the evolution of the structure of the superconducting instabilities when λ_R, λ_I , and D_0 are turned on. As follows from Table I and as summarized in Fig. 4(a), depending on which combination of these three parameters is nonzero, the system exhibits a variety of point groups. This is important for pairing since certain order parameter configurations, corresponding to distinct IRs of the point group $C_{6h} \times \text{SO}(3)_s$ of the system at $\lambda_R = \lambda_I = D_0 = 0$, can mix when the symmetry group is reduced.

To define the superconducting order parameter, we use the electronic operators $c_{k,\eta,s}^\dagger$ introduced in Sec. II B, which create an electron with momentum $\mathbf{k} \in \text{MBZ}$ in the band in valley η and of spin s that is closest to the Fermi level in the limit $\lambda_R = \lambda_I = D_0 = 0$. The representations of the symmetries in this basis are listed in Table I (which fixes their phase ambiguity). Focusing as before on the energetically most favorable intervalley pairing, the order parameter reads as

$$\mathcal{H}_{\text{SC}} = \sum_{k,s,s',\eta} \sum_{\mu=0}^3 c_{k,\eta,s}^\dagger [(d_{k,\eta})_\mu s_\mu i s_y]_{s,s'} c_{-k,-\eta,s'}^\dagger + \text{H.c.}, \quad (12)$$

where

$$(d_{k,\eta})_0 = (d_{-k,-\eta})_0 \text{ and } (d_{k,\eta})_j = -(d_{-k,-\eta})_j, \quad (13)$$

$j = x, y, z$, are the singlet and triplet components of the order parameter, respectively. Let us start in the limit $\lambda_R = \lambda_I = D_0 = 0$. As the point group $C_{6h} \times \text{SO}(3)_s$ contains spin rotation symmetry, spin singlet and spin triplet cannot mix. Furthermore, we expect the dominant pairing to involve Cooper pairs of electrons of the same mirror-symmetry (σ_η)

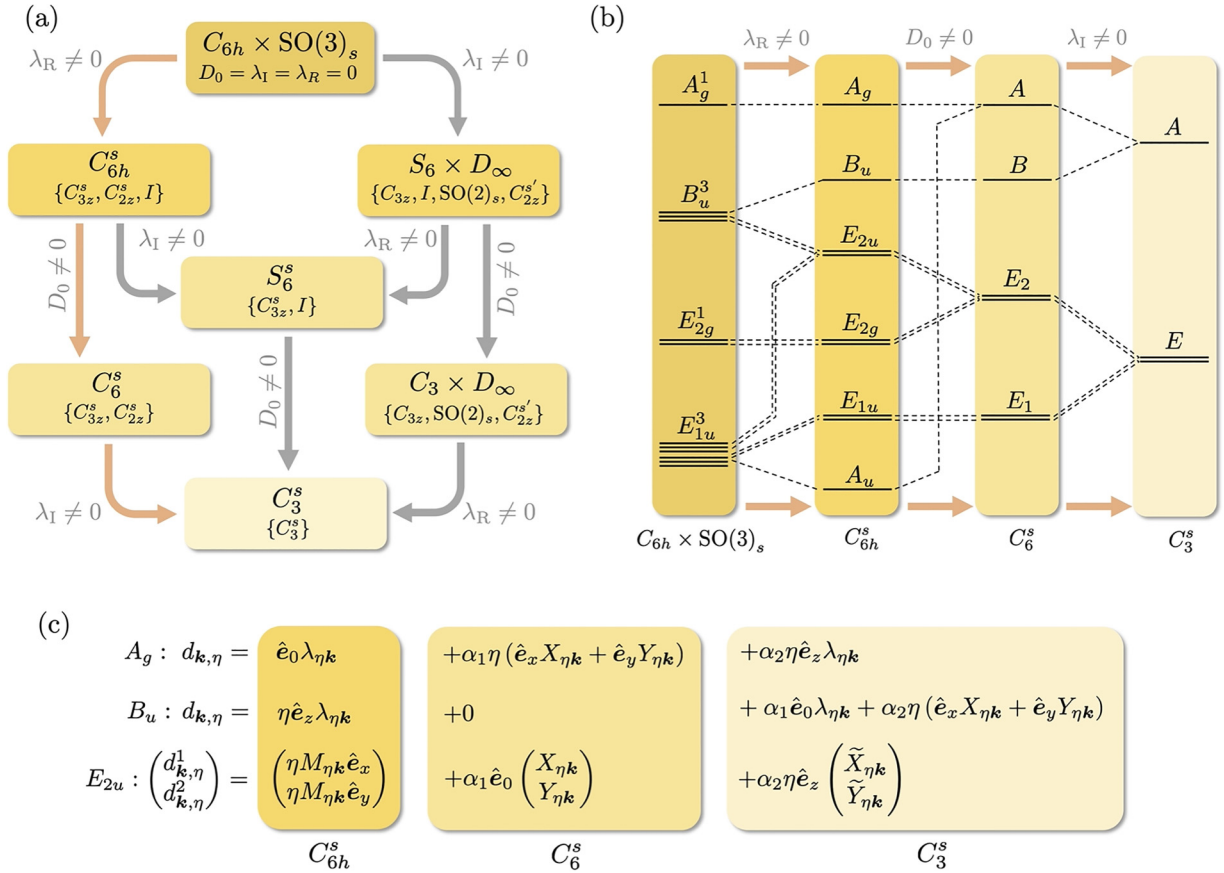


FIG. 4. (a) Summary of point groups when D_0 , λ_R , and λ_I are turned on, focusing for concreteness on geometry (i) in Eq. (5); the modifications for geometry (ii) follow from Table I. We also list a (in many cases redundant) set of generators, see Table I for the definitions and representations of the symmetry operations. We use D_∞ to refer to the group generated by $\{SO(2)_s, C_{2z}^s\}$. Choosing one specific path [indicated in light red in (a)] as an example, we show in (b) the evolution of the IRs of the pairing states. For the superconducting states emerging out of A_g^1 and B_u^3 , we summarize their order parameters in (c). To keep the notation compact we use the four-component basis vectors $(\mathbf{e}_\mu)_{\mu'} = \delta_{\mu,\mu'}$.

sector and not between different sectors, leading to pairing being even under σ_h . In fact our low-energy description of pairing in Eq. (12) automatically implies that: in the presence of σ_h , every band has a distinct eigenvalue under σ_h and the band in a given valley η closest to the Fermi level at momentum \mathbf{k} , where an electron is created by application of $c_{\mathbf{k},\eta,s}^\dagger$, has the same σ_h eigenvalue as the band closest to the Fermi level at $-\mathbf{k}$ and $-\eta$. Since the Fermi-Dirac constraint (13) further implies [70] that singlet (triplet) is even (odd) under C_{2z} and I , we are left with the IRs A_g or E_{2g} of C_{6h} for singlet and B_u or E_{1u} for triplet pairing.

A. Pairing in one-dimensional IRs of C_{6h}

Let us first focus on the one-dimensional IRs, A_g and B_u , i.e., pairing transforming trivially under C_{3z} ; to indicate their respective spin-structure, these states are represented by A_g^1 and B_u^3 in Fig. 4(b). They have the following order parameters:

$$A_g^1: d_{\mathbf{k},\eta} = (\lambda_{\eta\mathbf{k}}; 0, 0, 0), \quad (14)$$

$$B_u^3: d_{\mathbf{k},\eta} = (0; \eta \lambda_{\eta\mathbf{k}} \hat{\mathbf{n}}), \quad (15)$$

where $\lambda_{\mathbf{k}} = \lambda_{C_{3z}\mathbf{k}} \in \mathbb{R}$ and $\hat{\mathbf{n}}$ is a real unit vector (here and in the following, we employ the slight abuse of notation where

the symbol C_{3z} refers both to the transformation as a group element and to its vector representation).

There are several orders of turning on the perturbations λ_R , λ_I , D_0 , corresponding to the different paths (arrows) in Fig. 4(a). As it is most important for our discussion here, we will focus on geometry (i) in Eq. (5) and λ_R being turned on first and then D_0 as an example [path in light red in Fig. 4(a)]; the generalization to other paths is straightforward. First, setting $\lambda_R \neq 0$ will reduce the point group to C_{6h}^s , where all symmetry operations in C_{6h} are replaced by appropriate combinations of spatial and spin transformations, i.e., the (redundant) generators C_{3z} , C_{2z} , and σ_h of C_{6h} are replaced by their spinful counterparts C_{3z}^s , C_{2z}^s , and σ_h^s , see Table I. Importantly, C_{6h}^s still contains $I = C_{2z}^s \sigma_h^s$ such that singlet and triplet continue to transform under different IRs and, hence, cannot mix. While the singlet is unaffected, the B_u^3 triplet splits into a state with triplet vector pinned along the s_z direction (as a consequence of C_{2z}^s) transforming under the one-dimensional IR B_u of C_{6h}^s and a doublet transforming under the two-dimensional IR E_{2u} ; their order parameters read as

$$B_u: d_{\mathbf{k},\eta} = (0; 0, 0, \eta \lambda_{\eta\mathbf{k}}), \quad (16)$$

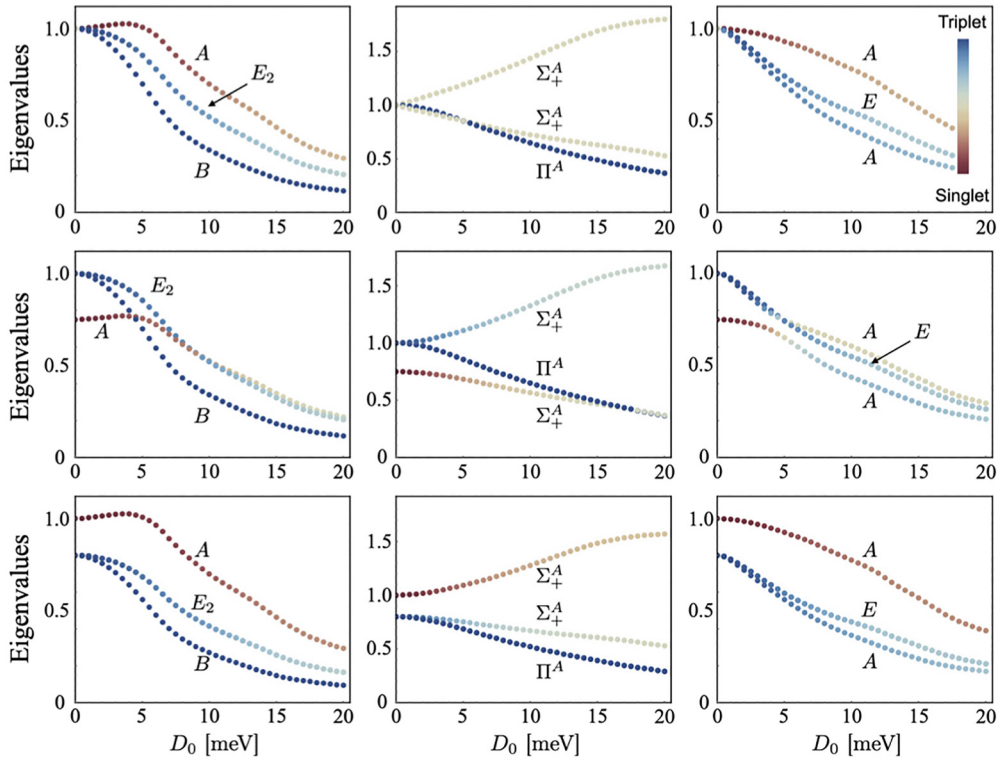


FIG. 5. Eigenvalues [normalized to unity at $D_0 = 0$] as a function of D_0 , (left column) $\lambda_R = 30$ meV; (middle column) $\lambda_L = 30$ meV; and (right column) $\lambda_L = \lambda_R = 30$ meV. The distinct IRs are indicated, see Fig. 4(b) for left and right column. When $\lambda_R = 0$, $\lambda_L \neq 0$ (middle column), the point group is $C_3 \times D_\infty$, see Fig. 4(a); we denote the two-dimensional (one-dimensional) IR which is trivial in C_3 and transforms as x, y (also trivial) under D_∞ by Π^A (Σ_+^A). (Top) SO(4) symmetric parent state, i.e., $\delta\gamma = 0$ in Eq. (9). (Middle) Spin-triplet favored parent state, with interaction $\delta\gamma = -0.25$. (Bottom) Spin-singlet favored parent state, with interaction $\delta\gamma = 0.25$. Everywhere the Fermi energy is $\varepsilon_F = 9.6$ meV.

$$E_{2u} : \begin{pmatrix} d_{k,\eta}^1 \\ d_{k,\eta}^2 \end{pmatrix} = \begin{pmatrix} (0; \eta M_{\eta k} \hat{e}_x, 0) \\ (0; \eta M_{\eta k} \hat{e}_y, 0) \end{pmatrix}, \quad (17)$$

where M_k is a real, 2×2 matrix, obeying $C_{3z}^{-1} M_{C_{3z}k} C_{3z} = M_k$. Naturally, for the E_{2u} state emerging out of and being close to the B_u^3 (and its descendent below), we expect $M_k \simeq \sigma_0 \lambda_k$; this is indeed what we see in the numerics (cf. first two rows in Fig. 6).

When also D_0 is nonzero, σ_h^s is broken and the point group is reduced to C_6^s . As it does not contain inversion symmetry I (nor C_{2z}) anymore, spin-singlet and triplet can now mix. More precisely, the presence of C_{2z}^s guarantees that the triplet component admixed to the singlet only contains in-plane spin components; the A_g singlet now becomes the A state of C_6^s with order parameter

$$A : d_{k,\eta}^A = (\lambda_{\eta k}; 0, 0, 0) + \alpha_1 \eta (0; X_{\eta k}, Y_{\eta k}, 0), \quad (18)$$

where X_k, Y_k are real-valued, MBZ-periodic functions transforming as k_x, k_y under C_{3z} [such as the two components of the spin-orbit vector \mathbf{g}_k in Eq. (31)]; we distinguish X_k, Y_k , which are generic functions, from the specific choice $\mathcal{X}_k, \mathcal{Y}_k$ of (10). Here $\alpha_1 \in \mathbb{R}$ describes the strength of the triplet admixture (coming from A_u of C_{6h}^s).

By the same token, C_{2z}^s prevents the B_u triplet in Eq. (16) to exhibit singlet or in-plane triplet components and, thus, remains of the same form; it will be relabeled as the B state

of C_6^s . Being even under C_{2z}^s , the E_{2u} doublet in Eq. (17), however, can mix with a singlet component (coming from E_{2g} of C_{6h}^s) and becomes the E_2 state of C_6^s with order parameter

$$E_2 : \begin{pmatrix} d_{k,\eta}^1 \\ d_{k,\eta}^2 \end{pmatrix} = \begin{pmatrix} (0; \eta M_{\eta k} \hat{e}_x, 0) \\ (0; \eta M_{\eta k} \hat{e}_y, 0) \end{pmatrix} + \alpha_2 \begin{pmatrix} (X_{\eta k}; \mathbf{0}) \\ (Y_{\eta k}; \mathbf{0}) \end{pmatrix}. \quad (19)$$

Finally, let us also take λ_1 to be finite, which breaks C_{2z}^s leaving us with the point group C_3^s , just consisting of spinfull threefold rotations along the z axis. Since the subduced representations of A and B of C_6^s onto C_3^s are both A of C_3^s , the singlet A in Eq. (18) and the out-of-plane triplet in Eq. (16) hybridize and become a single phase with order parameter ($\beta \in \mathbb{R}$)

$$A : d_{k,\eta} = (\lambda_{\eta k}; \mathbf{0}) + \alpha_1 \eta (0; X_{\eta k}, Y_{\eta k}, 0) + \beta (0; \eta \lambda_{\eta k} \hat{e}_z). \quad (20)$$

The broken C_{2z}^s also allows for more terms in the previous E_2 state in Eq. (19) which now also exhibits a spin component along the out-of-plane direction (coming from E_1 of C_6^s),

$$E : \begin{pmatrix} d_{k,\eta}^1 \\ d_{k,\eta}^2 \end{pmatrix} = \begin{pmatrix} (0; \eta M_{\eta k} \hat{e}_x, 0) \\ (0; \eta M_{\eta k} \hat{e}_y, 0) \end{pmatrix} + \alpha_2 \begin{pmatrix} (X_{\eta k}; \mathbf{0}) \\ (Y_{\eta k}; \mathbf{0}) \end{pmatrix} + \alpha_3 \eta \begin{pmatrix} (0; \tilde{X}_{\eta k} \hat{e}_z) \\ (0; \tilde{Y}_{\eta k} \hat{e}_z) \end{pmatrix}, \quad (21)$$

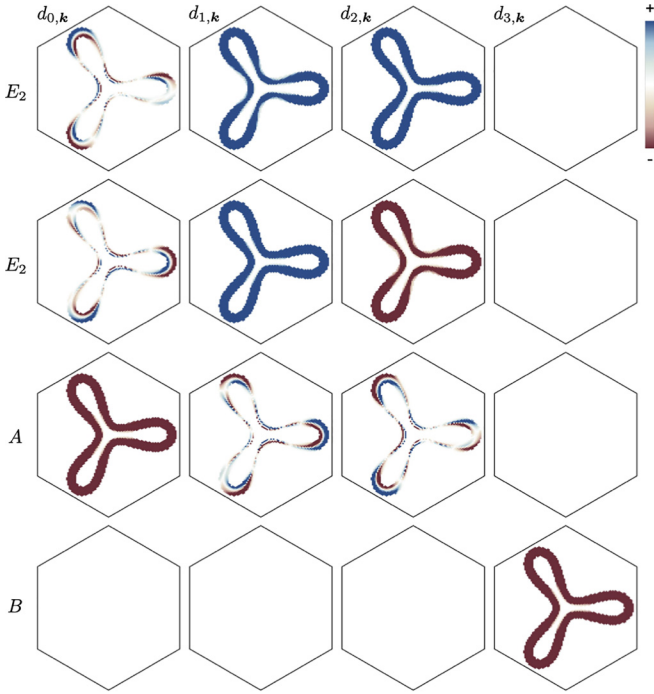


FIG. 6. Spin-triplet favored parent state, i.e., $\delta\gamma/\gamma_0 = -0.25$, with fixed $D_0 = 6$ meV, $\lambda_R = 30$ meV, $\lambda_I = 0$ and $\varepsilon_F = 9.6$ meV. (Top-to-bottom) Corresponds to leading eigenvalue down to fourth eigenvalue; the corresponding IRs are labeled.

where the tilde of \tilde{X} and \tilde{Y} in the last term just indicates that these functions need not be identical to X and Y but exhibit the same transformation behavior. The admixture of the different IRs of the respective point groups and the form of the pairing states discussed here are summarized schematically in Figs. 4(b) and 4(c), respectively.

B. Two-dimensional IRs of C_{6h}

While all of the states above can and are generically expected to be fully gapped, recent experiments [60,61] indicate that also nodal pairing can be realized in graphene moiré systems. For this reason, we next discuss pairing emerging out of the remaining, two-dimensional IRs— E_{2g} and E_{1u} of C_{6h} . As discussed above already, they are pure singlet and triplet states, respectively, in the presence of inversion symmetry. We begin with the singlet, E_{2g}^1 , with order parameter

$$E_{2g}^1 : \begin{pmatrix} d_{k,\eta}^1 \\ d_{k,\eta}^2 \end{pmatrix} = \begin{pmatrix} (X_{\eta k}; 0, 0, 0) \\ (Y_{\eta k}; 0, 0, 0) \end{pmatrix}. \quad (22)$$

The associated nematic superconducting state, $(d_{k,\eta})_\mu = \delta_{\mu,0} X_{\eta k}$, can have stable nodal points (depending on the Fermi surface), while the chiral state, $(d_{k,\eta})_\mu = \delta_{\mu,0} (X_{\eta k} + iY_{\eta k})$, will generically be fully gapped. Finite λ_R does not change the form of the order parameter since I (of C_{6h}^s) prohibits any triplet admixture. However, when also D_0 is finite, the E_{2g} and E_{2u} states of C_{6h}^s can hybridize into the E_2 state of C_6^s ,

$$\begin{pmatrix} d_{k,\eta}^1 \\ d_{k,\eta}^2 \end{pmatrix} = \begin{pmatrix} (X_{\eta k}; 0, 0, 0) \\ (Y_{\eta k}; 0, 0, 0) \end{pmatrix} + \alpha_1 \begin{pmatrix} (0; \eta M_{\eta k} \hat{e}_x, 0) \\ (0; \eta M_{\eta k} \hat{e}_y, 0) \end{pmatrix}. \quad (23)$$

By design, the form of this state is equivalent to that in Eq. (19) discussed above. However, there are a few important differences in the precise nature of it: if the E_{2g}^1 state dominates at $\lambda_R = \lambda_I = D_0 = 0$, then turning on λ_R , D_0 weakly will lead to a small admixture of the second term in Eq. (23) to the first. Furthermore, as opposed to Eq. (19), there is no reason anymore that $M_{\eta k}$ in Eq. (23) is close to $\sigma_0 \lambda_k$ with λ_k that is approximately constant on the Fermi surface. And, indeed, we find a nontrivial M_k in our numerics below.

Finally, the triplet E_{1u}^3 has a matrix-valued order parameter,

$$d_{k,\eta}^{i,j} = \eta \begin{pmatrix} X_{\eta k} \\ Y_{\eta k} \end{pmatrix} \hat{e}_i, \quad i = x, y, z, \quad j = 1, 2, \quad (24)$$

which leads to a multitude of possible phases in the absence of SOC [70]. When λ_R is turned on, it splits into

$$A_u : d_{k,\eta} = \eta(0; X_{\eta k}, Y_{\eta k}, 0), \quad (25)$$

$$E_{1u} : \begin{pmatrix} d_{k,\eta}^1 \\ d_{k,\eta}^2 \end{pmatrix} = \eta \begin{pmatrix} (0; X_{\eta k} \hat{e}_z) \\ (0; Y_{\eta k} \hat{e}_z) \end{pmatrix}, \quad (26)$$

and another E_{2u} component that mixes with the B_u^3 state [absorbed in M_k in Eq. (17)]. If also D_0 is finite, the A_u state will mix with the A_g state leading to the A superconducting order parameter of C_6^s in Eq. (18). Interestingly, the E_{1u} state of C_{6h}^s simply becomes the E_1 state of C_6^s without any changes to its form. Finally, for finite λ_I , the E_1 and E_2 phases of C_6^s mix and become the E state of C_3^s with order parameter of the form of Eq. (21).

IV. SUPERCONDUCTING ENERGETICS

Our next objective is to explicitly compute the influence of D_0 and SOC on the various possible parent states. The numerical results will be directly related back to the symmetry classification of the previous section, and we will further appeal to analytic arguments, Sec IV C, to explain key features of our numerical findings.

A. Numerics for fully gapped states

Using the linearized gap equation (11) with vertex Γ^{even} given by the first line of Eq. (9), we compute the evolution of the superconducting order parameters, $d_{\mu,k} = (d_{k,\eta=\pm})_\mu$, under applied SOC and displacement field, as well as for the different spin-symmetries of the parent superconducting state. The leading eigenvalues are presented in Fig. 5 and selected eigenvectors can be found in Figs. 6 and 7. In these plots, we have set $\theta = 1.50^\circ$, $w_0/w_1 = 0.875$ (which are tunneling parameters defined in Appendix A), and taken the Fermi level at $\varepsilon_F = 9.5$ meV which corresponds to filling $\nu \simeq 3.25$ of the moiré bands. We note that in the closely related system—i.e., the single sided TMD/TTLG heterostructure of Ref. [26]—superconductivity is observed to be strongest in the range $2 < |\nu| < 4$ and trends towards $|\nu| \sim 4$ with increasing D_0 [see e.g., Fig. 1(c) of that work]. Finally, for the gap equation (11) we keep eight bands n (of a given valley) in the summation in $\mathcal{W}_{\mu\nu,p}$. We now comment on the key features of these results.

(1) Left column Fig. 5. At $\lambda_R \neq 0$ increasing D_0 generates a splitting of the states into the distinct IRs A, B, E_2 of C_6^s [cf.

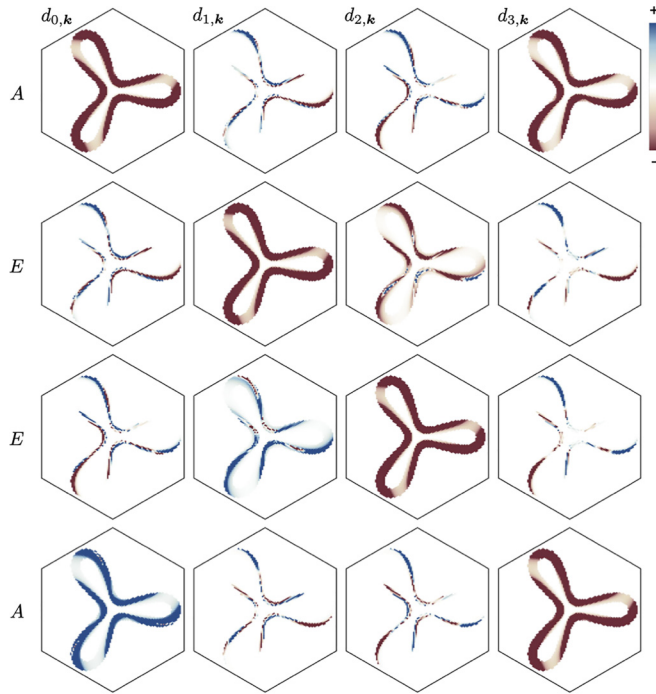


FIG. 7. Spin-triplet favored interaction $\delta\gamma/\gamma_0 = -0.25$, with fixed $D_0 = 6$ meV, $\lambda_R = \lambda_I = 30$ meV, and $\varepsilon_F = 9.6$ meV. (Top-to-bottom) Corresponds to leading eigenvalue down to fourth eigenvalue; the corresponding IRs are labeled.

Fig. 4(b)]. We see from Fig. 6 that the singlet A has admixed in-plane triplet character, while the in-plane triplet E_2 has admixed singlet character; the admixture increases with D_0 . The admixed components exhibit sign changes around the Fermi surface. The triplet B (nondegenerate eigenvector), however, remains a pure triplet with triplet vector pinned to the out-of-plane direction. These features are in perfect agreement with the symmetry analysis, see Eqs. (16), (18), and (19), and are further elucidated in Sec. IV C using a complementary description of the gap equation. That analysis will also explain why the admixed singlet (triplet) component(s) of the E_2 (A) state change sign between the two Fermi surfaces.

(2) Middle row, left column Fig. 5. For the case of the triplet preferred parent state $\delta\gamma < 0$, and with $\lambda_R \neq 0$, we see that the leading eigenvalue exhibits a change from E_2 to A at $D_0 \simeq 9$ meV for $\lambda_R = 30$ meV. Since all three states transform according to different IRs, their eigenvalues cross each other (rather than exhibit avoided crossings), which corresponds to a phase transition. However, the precise form of the phase diagram—with or without phase coexistence—goes beyond the linearized gap equation and will be discussed in Sec. IV B below.

(3) Middle Column Fig. 5. At $\lambda_I \neq 0$ increasing D_0 generates a splitting of the states into the distinct IRs Σ_+^A , Π^A of $C_3 \times D_\infty$, with two nondegenerate states belonging to Σ_+^A , which correspond to the symmetric and antisymmetric combinations, i.e., $d_{0,k} \pm d_{3,k}$.

(4) Right Column Fig. 5. At $\lambda_R, \lambda_I \neq 0$ increasing D_0 generates a splitting of the states into the distinct IRs A, E of C_3^s , again with two nondegenerate states belonging to A . These two nondegenerate states can be thought of as the “bonding”

and “anti-bonding” configurations of the A and B states of C_6^s in Fig. 4(b). This is confirmed by noting in the first (last) row in Fig. 7 that the two singlet states A have symmetric (antisymmetric) combinations of $d_{0,k}$ and $d_{3,k}$, i.e., different signs of β in Eq. (20). This hybridization is also visible in the D_0 dependence of the eigenvalues in the last column of Fig. 5, which exhibits an avoided crossing between the associated pair of eigenvalues. The A states also have admixed in-plane triplet character, with sign changes around the Fermi surface. On the other hand, the in-plane triplet E (the second and third rows of Fig. 7) has admixed $d_{0,k}$ and $d_{3,k}$, which exhibit sign changes on the Fermi sheets. These features are well explained by the symmetry arguments [cf. Eqs. (20) and (21)].

B. Phase transition

As already mentioned above, the crossing at a critical value $D_0 = D_0^c$ between the leading and subleading eigenvalues in the middle row, left column panel in Fig. 5 implies that there is a transition from the (E_2 of C_6^s) in-plane triplet with admixed singlet component in Eq. (19) to the singlet with admixed in-plane triplet components of Eq. (18), transforming as A of C_6^s . The linearized gap equation, however, does not yet fully determine the phase diagram in the vicinity of D_0^c and T_c . To discuss this further, we expand the superconducting order parameter in Eq. (12) as

$$d_{k,\eta} = \Psi d_{k,\eta}^A + \sum_{j=1,2} \phi_j d_{k,\eta}^j, \quad \Psi, \phi_j \in \mathbb{C}, \quad (27)$$

where $d_{k,\eta}^A$ and $d_{k,\eta}^j$ are given by the four-component vectors in Eqs. (18) and (19), respectively. Considering terms up to quartic order in Ψ and $\phi = (\phi_1, \phi_2)$ that are consistent with the C_6^s point group, time-reversal, and gauge invariance, the free-energy must have the form

$$\begin{aligned} \mathcal{F} \sim & \frac{1}{2} a_A |\Psi|^2 + \frac{1}{2} a_{E_2} \phi^\dagger \phi + \frac{1}{4} b_A |\Psi|^4 + \frac{1}{4} b_{E_2,1} (\phi^\dagger \phi)^2 \\ & + \frac{1}{4} b_{E_2,2} |\phi^T \phi|^2 + \frac{1}{2} c_1 |\Psi|^2 \phi^\dagger \phi + \frac{1}{2} c_2 \text{Re}[\Psi^2 \phi^\dagger \phi^*] \end{aligned} \quad (28)$$

close to T_c . Before proceeding, we first obtain an estimate for the real-valued coefficients of the quartic terms, $b_A, b_{E_2,1}, b_{E_2,2}, c_1, c_2$; we take the effective two-band normal-state Hamiltonian in Eq. (6), neglect the spin splitting, $\mathbf{g}_k = 0$, and integrate out the fermions coupled to the superconducting order parameters Ψ, ϕ via Eqs. (27) and (12). Further neglecting the small admixture, $\alpha_{1,2} = 0$, and taking $\lambda, M = \text{const.}$ in Eqs. (18) and (19), we find

$$b_A = b_{E_2,1}/2 = -b_{E_2,2} = c_1/2 = c_2 > 0, \quad (29)$$

where $b_A = 64 \sum_{\omega_n} \int \frac{d^2k}{(2\pi)^2} (\omega_n^2 + \xi_k^2)^{-2}$. Most importantly, we see that $b_{E_2,2} < 0$, favoring the unitary (nematic E_2) state, $\phi \propto \hat{e}_1$, over the nonunitary (chiral E_2) configuration, $\phi \propto \hat{e}_1 + i\hat{e}_2$, where $\hat{e}_{1,2}$ are two orthogonal two-component unit vectors. Minimizing the free energy in Eq. (28) for $b_{E_2,2} < 0$, one finds that depending on

$$\gamma = \frac{c_1 - |c_2|}{\sqrt{b_A (b_{E_2,1} + b_{E_2,2})}}, \quad (30)$$

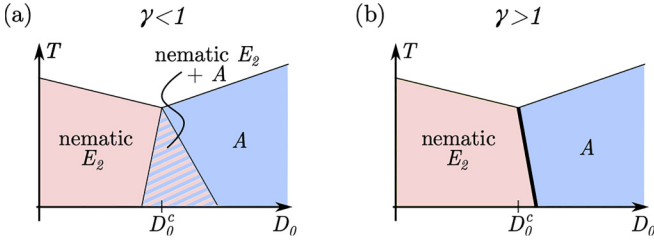


FIG. 8. For $b_{E_2,2} < 0$, we either get (a) an intermediate region of microscopic coexistence or (b) a first order transition between the two superconductors, depending on the value of γ in Eq. (30).

one either obtains microscopic coexistence of Ψ and nematic ϕ ($\gamma < 1$) or a first-order transition between the two ($\gamma > 1$), see Fig. 8. Interestingly, for the approximate estimate in Eq. (29) we get $\gamma = 1$ and these two possibilities are degenerate. As such, additional corrections coming from nontrivial form factors ($\lambda, M \neq \text{const.}$), SOC, and fluctuation-[70,72,73] or disorder [74] corrections can determine which of the two scenarios in Fig. 8 is realized. In the case of microscopic coexistence, $\gamma < 1$, the relative phase of Ψ and ϕ_j is determined by the sign of c_2 . For the positive sign of c_2 obtained from our estimate in Eq. (29), we find $\phi^* \Psi$ to be purely imaginary, such that the superconducting state in the hatched region in Fig. 8(a) breaks time-reversal symmetry.

We note that significant corrections to Eq. (29), e.g., resulting from strong ferromagnetic fluctuations [70], can change the sign of $b_{E_2,2}$. Positive $b_{E_2,2}$ will favor $\phi \propto \hat{e}_1 + i\hat{e}_2$ for sufficiently small D_0 . However, close to $D_0 = D_0^c$, the competition between the terms $\propto b_{E_2,2}$ and $\propto c_2$ in Eq. (28) will lead to more complex behavior than in Fig. 8: depending on parameters, we find (not shown) either no coexistence, or coexistence with a first order transition, or a coexistence region with two different regimes (coexistence with only nematic or nematic and chiral pairing).

Since the transition involves superconducting states with different symmetries, there should be multiple ways of probing it experimentally. Given the current experimental status in graphene moiré systems, we believe that the most straightforward way proceeds by measuring the variation of the superconducting critical temperature T_c as a function of magnetic field \mathbf{B} and displacement field D_0 : the order parameter of the A state does not allow to construct a time-reversal-odd, gauge-invariant composite order parameter and, hence, cannot couple linearly to the magnetic field \mathbf{B} (even in the presence of strain). This is different for the E_2 order parameter since we can define $i(\phi_1^* \phi_2 - \phi_2^* \phi_1)$, which transforms in the same way as the magnetic field component along the out-of-plane z direction; it can, hence, couple linearly to it. In the presence of strain, it can also couple linearly to the in-plane magnetic field components. Consequently, the behavior of $T_c(\mathbf{B})$ is very different in the two phases and we therefore expect a drastic change of it when D_0 changes across the transition, making it directly observable.

C. Character of the admixed state

To further supplement the numerical studies of the gap equation (11), here we provide a complementary analysis to

elucidate key features of the superconducting order parameters $(d_{k,\eta})_\mu$. We specialize to $\lambda_R, D_0 \neq 0$ for this analysis.

We describe the behavior of the eigenvectors of the gap equation (11) in terms of the effective $\mathbf{g}_{\eta k}$ vector in Eq. (6), which captures the impact of SOC (and D_0) on the partially filled moiré bands at the Fermi level. The $\mathbf{g}_{\eta k}$ vector can be explicitly computed from the full continuum model and its form can be inferred from Fig. 2. Recasting the mean-field Hamiltonian (8) in terms of $\mathbf{g}_{\eta k}$ and separating $\mathcal{H}_\eta = \mathcal{H}_\eta^{(0)} + \mathcal{H}_\eta^{(1)}$,

$$\mathcal{H}_\eta^{(0)} = \sum_{k,s,s'} [\xi_{\eta k} s_0 + \eta \mathbf{g}_{\eta k} \cdot \mathbf{s}]_{s,s'} c_{k,s,\eta}^\dagger c_{k,s',\eta} \quad (31)$$

$$\begin{aligned} \mathcal{H}_\eta^{(1)} = & \sum_{k_1,k_2;\mu,\nu} (-\Gamma^{-1})_{k_1,k_2;\mu,\nu} (d_{k_1,\eta}^*)_\mu (d_{k_2,\eta})_\nu \\ & + \sum_{k;s_1,s_2;\mu} \{c_{\eta,n,k}^\dagger c_{\eta,n',-k}^\dagger [(d_{k,\eta})_\mu (s_{\mu} i s_{\nu})_{s_1,s_2}] + \text{H.c.}\}. \end{aligned} \quad (32)$$

The eigenvalues of $\mathcal{H}_\eta^{(0)}$ are $E_{\pm,\eta k} = \xi_{\eta k} \pm |\mathbf{g}_{\eta k}|$ and the subsequent normal-state Greens function is conveniently expressed as

$$G_{k,i\omega_n}^{\eta,\eta'} = [G_{\eta k,i\omega_n}^+ s_0 + \eta \hat{\mathbf{g}}_{\eta k} \cdot \mathbf{s} G_{\eta k,i\omega_n}^-] \delta_{\eta,\eta'}, \quad (33)$$

with $\hat{\mathbf{g}}_{\eta k} = \mathbf{g}_{\eta k}/|\mathbf{g}_{\eta k}|$ and

$$G_{\eta k,i\omega_n}^\pm = \left[\frac{1}{i\omega_n - E_{+,\eta k}} \pm \frac{1}{i\omega_n - E_{-,\eta k}} \right]. \quad (34)$$

We consider an interaction vertex in the superconducting channel, $\Gamma_{k,k';\mu\nu} = \Gamma_{k,k'}^0 \delta_{\mu\nu}$, which strictly favors intervalley pairing, and which is even in the quasimomentum indices, i.e., $\Gamma_{k,k'}^0 = \Gamma_{-k,-k'}^0 = \Gamma_{k,-k'}^0 = \Gamma_{-k,k'}^0$; to be explicit we take the interaction as given by the first line in Eq. (9) in the limit $\delta\gamma = 0$. Utilizing that the Greens function is diagonal in valley indices, as per Eq. (33), the linearized gap equation reads

$$\begin{aligned} (\Delta_k^{\eta,-\eta})_{s,s'} = & T \sum_{n,k';s_1,s_2;\eta} \Gamma_{k,k'}^0 (G_{k',i\omega_n}^{\eta,\eta})_{s,s_1} \\ & \times (\Delta_{k'}^{\eta,-\eta})_{s_1,s_2} (G_{-k',-i\omega_n}^{-\eta,-\eta})_{s',s_2}. \end{aligned} \quad (35)$$

As before in Sec. IV A, we specialize to a given $\eta = +$ and denote $d_{\mu,k} = (d_{k,+})_\mu$ such that the decomposition into the spin-singlet and triplet components is,

$$\Delta_k^{+-} = d_{0,k} s_0 + \mathbf{d}_k \cdot \mathbf{s}. \quad (36)$$

The gap equation (35) reduces to

$$\begin{aligned} d_{0,k} = & \sum_{k'} \Gamma_{k,k'}^0 [\mathbb{V}_{T,k}^+ d_{0,k'} + \mathbb{V}_{T,k}^- \hat{\mathbf{g}}_k \cdot \mathbf{d}_{k'}], \\ \mathbf{d}_k = & \sum_{k'} \Gamma_{k,k'}^0 [\mathbb{V}_{T,k}^+ \mathbf{d}_{k'} + \mathbb{V}_{T,k}^- \hat{\mathbf{g}}_k d_{0,k'} \\ & + 2\mathbb{V}_{T,k}^0 [\hat{\mathbf{g}}_k (\hat{\mathbf{g}}_{k'} \cdot \mathbf{d}_{k'}) - \mathbf{d}_{k'}]]. \end{aligned} \quad (37)$$

We have defined the sums and differences of thermal occupation factors,

$$\mathbb{V}_{T,k}^\pm = \frac{1}{2} T \sum_n \left[\frac{1}{E_{+,k}^2 + \omega_n^2} \pm \frac{1}{E_{-,k}^2 + \omega_n^2} \right], \quad (38)$$

$$\mathbb{V}_{T,k}^0 = T \sum_n \frac{(E_{+,k} - E_{-,k})^2}{(E_{+,k}^2 + \omega_n^2)(E_{-,k}^2 + \omega_n^2)}. \quad (39)$$

To understand the important characteristics of the superconducting order parameters $d_{\mu,k}$, which we observed in Sec. IV A through a comprehensive numerical analysis of the gap equation (11), we will now present our analytic findings based on a perturbative expansion in $\mathbb{V}_{T,k}^-$. Specifically, we will examine the properties of the A and E_2 states and compare our results with the findings presented in Fig. 6. The explicit steps of the perturbative expansion are provided in Appendix C.

It is important, for what follows, to first establish the (approximate) equality

$$\mathbb{V}_{T,k_F^\pm}^\pm = \pm \mathbb{V}_{T,k_F^\mp}^\pm, \quad (40)$$

where we define k_F^\pm as points on the Fermi surfaces for the $E_{\pm,k}$ bands, i.e., $E_{\pm,k_F^\pm} = 0$. To this end, we assume $|\mathbf{g}_k|$ does not change between Fermi surfaces, i.e., $|\mathbf{g}_{k_F^\pm}| = |\mathbf{g}_{k_F^\mp}| \equiv |g|$. Next, employ a linear expansion of the dispersion in momentum normal to a point k_F on the Fermi surface of ξ_k , i.e., denoting the normal vector $\hat{n}_{k_F}^{FS}$, we expand in $\delta\mathbf{k} = (k - k_F^0)\hat{n}_{k_F}^{FS}$ such that $\xi_{\delta k} \simeq v(k - k_F^0)$. From $E_{\pm,k_F^\pm} = 0$ we see that $k_F^\pm = k_F^0 \pm |g|/v$ and so $E_{+,k_F^\pm}^2 = E_{-,k_F^\mp}^2 = 4|g|^2$; this implies $\mathbb{V}_{T,k_F^\pm}^\pm = \pm \mathbb{V}_{T,k_F^\mp}^\pm$.

A state. We start by considering the dominant singlet state $d_{0,k}$, with admixed in-plane triplet components $\mathbf{d}_k^\parallel = (d_{1,k}, d_{3,k})$ vector (and ignoring the $d_{3,k}$ component which is decoupled). Reinstating the valley index η , we denote the unperturbed (i.e., $\mathbb{V}_{T,k}^- \rightarrow 0$) A state as

$$d_{\eta,k}^A = (d_{0,\eta,k}^{(0)}; \mathbf{0}), \quad (41)$$

with $d_{0,\eta,k}^{(0)}$ approximately constant in \mathbf{k} . The perturbation $\mathbb{V}_{T,\eta,k}^-$ generates admixed triplet components,

$$d_{\eta,k}^A{}' = (d_{0,\eta,k}^{(0)}; \beta\eta\mathbb{V}_{T,\eta,k}^- \hat{\mathbf{g}}_{\eta,k}), \quad (42)$$

with β a dimensionless factor (see Appendix C for details). Since the two components of $\hat{\mathbf{g}}_{\eta,k}$ transform as k_x and k_y under C_{3z} , this is consistent with the form in Eq. (18) predicted by symmetry. Moreover, this simple expression already captures the key features clearly seen in the full numerical results in the third line of Fig. 6; the admixed triplet vector changes sign between the spin split Fermi surfaces due to the factor $\mathbb{V}_{T,\eta,k}^-$ and Eq. (40). We further see that it inherits the directional dependence of $\hat{\mathbf{g}}_{\eta,k}$, including its Möbius texture [59] for $\lambda_1 \ll \lambda_R$, see Fig. 2(b).

E_2 states. Similar to above, we denote the unperturbed (i.e., $\mathbb{V}_{T,\eta,k}^- \rightarrow 0$) E_2 state as

$$d_{\eta,k}^{E_2} = (0; \eta\mathbf{d}_{\eta,k}^{(0)}), \quad (43)$$

where, to a good approximation, $\mathbf{d}_{\eta,k}^{(0)} \simeq \mathbf{e}_\parallel$, with \mathbf{e}_\parallel a constant in-plane vector, for all \mathbf{k} such that $\Theta_{\mathbf{k};\varepsilon_F} = 1$, i.e., in the grid of Fig. 3. The perturbation $\mathbb{V}_{T,\eta,k}^-$ generates admixed singlet components,

$$d_{\eta,k}^{E_2}{}' = (\beta\mathbb{V}_{T,\eta,k}^- \eta\hat{\mathbf{g}}_{\eta,k} \cdot \mathbf{e}_\parallel; \eta\mathbf{d}_{\eta,k}^{(0)}), \quad (44)$$

This first-order perturbation expansion already captures the key features observed in the E_2 states presented in Fig. 6; the admixed singlet component changes sign between the spin split Fermi surfaces due to the factor $\mathbb{V}_{T,\eta,k}^-$ obeying Eq. (40) and further inherits the directional dependence of $\hat{\mathbf{g}}_{\eta,k} \cdot \mathbf{e}_\parallel$.

D. Nodal pairing

In this final section, we start from a nodal parent state and examine its characteristics under applied D_0 and SOC. To this end, Fig. 9 illustrates the evolution of the distinct IRs as the singlet-triplet interaction-asymmetry parameter $\delta\gamma$ in Eq. (9) is varied. The numerical results of Fig. 9 are obtained from the gap equation (11) by using the odd-vertex $\Gamma_{k_1,k_2;\mu,\nu}^{\text{odd}}$ of Eq. (9), which enables nodal pairing. As can be seen from the eigenvalues, the system is in an E_2 state at $\delta\gamma/\gamma_0 = 0$, and subsequently undergoes a crossing with an A state (signaling a phase transition, cf. Sec. IV B) as $-\delta\gamma/\gamma_0$ is increased. The dominant eigenvector(s) at each limit of $\delta\gamma/\gamma_0$ are also shown—and demonstrate a switch in behavior from a singlet-dominant E_2 state to that of a triplet-dominant A state. To complete our analysis of the nodal pairing, we detail the structure of each of the distinct states $\{A, A, E_2, E_2, E_1\}$ of Fig. 9, focusing on the region $\delta\gamma/\gamma_0 \simeq -0.025$. We show how the order parameter structures relate to the known vectors of the system, i.e., the $\mathbf{g}_{\eta k}$ coming from SOC; the $(\mathcal{X}_{\eta k}, \mathcal{Y}_{\eta k})$ coming from the interaction vertex Eq. (9); and the vector triad $\{\hat{\mathbf{e}}_x, \hat{\mathbf{e}}_y, \hat{\mathbf{e}}_z\}$ for the spin-triplet components.

A states. Considering the first (highest eigenvalue) A state of Fig. 9 at $\delta\gamma/\gamma_0 \simeq -0.025$, the numerical solution reveals the following structure:

$$d_{k,\eta} = \beta (\lambda_{\eta k}; 0, 0, 0) + \eta(0; \mathcal{X}_{\eta k}, \mathcal{Y}_{\eta k}, 0). \quad (45)$$

Here $\lambda_{\eta k}$ is not close to the identity, but is instead approximately of the form $\lambda_{\eta k} \simeq \mathbf{g}_{\eta k} \cdot (\mathcal{X}_{\eta k}, \mathcal{Y}_{\eta k})\mathbb{V}_{T,\eta,k}^-$, which transforms like a scalar under three-fold rotations. As a reminder, the function $\mathbb{V}_{T,\eta,k}^-$ changes sign between the two Fermi surfaces, see Eq. (40), and β is a small dimensionless parameter. Meanwhile, the second highest A state of Fig. 9 takes a rather different form

$$d_{k,\eta} = \beta (\tilde{\lambda}_{\eta k}; 0, 0, 0) + \eta(0; \mathcal{Y}_{\eta k}, -\mathcal{X}_{\eta k}, 0). \quad (46)$$

Here $\tilde{\lambda}_{\eta k} \simeq \mathbf{g}_{\eta k} \cdot (\mathcal{Y}_{\eta k}, -\mathcal{X}_{\eta k})\mathbb{V}_{T,\eta,k}^-$ is again a scalar under three-fold rotations and the triplet components of (46) are seen to be simply a $\pi/2$ -rotation relative to those of (45). These two A states can be understood as resulting from the rotationally trivial combination of $(\mathcal{X}_{\eta k}, \mathcal{Y}_{\eta k})$ with each of the two components of the nodeless E_2 state of Fig. 6. Within our symmetry analysis in Sec. III B, they correspond to the admixture of A_g to A_u in Eq. (25), see Fig. 4(b). This is consistent with triplet being dominant in both Eqs. (45) and (46), while the singlet components are admixed. As per our discussion in Sec. IV C the admixed components exhibit sign changes between the Fermi surfaces.

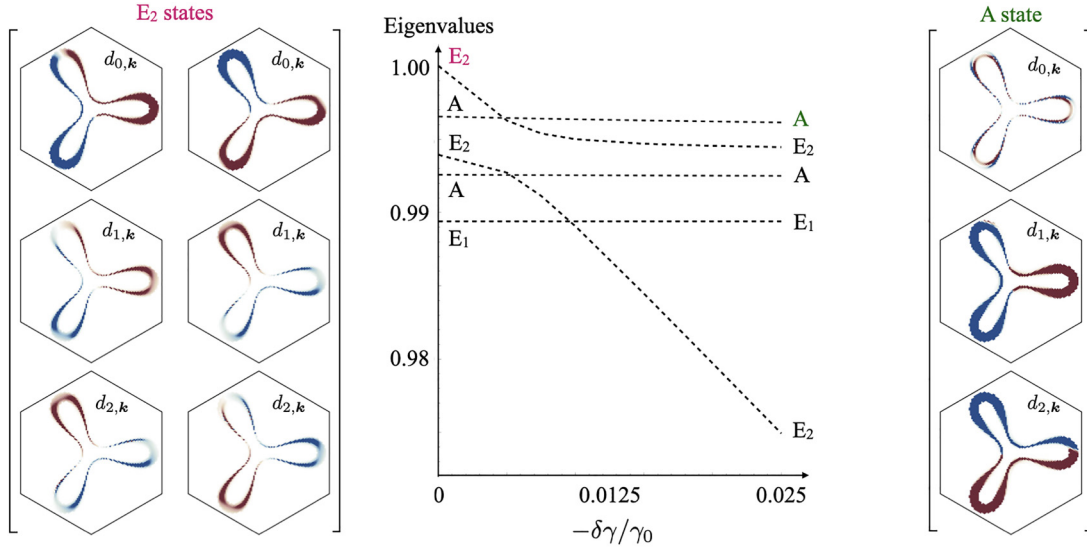


FIG. 9. Nodal pairing: states and their evolution with $\delta\gamma$. Dashed lines are the eigenvalues obtained by direct computation of the gap equation (11). Eigenvectors for the leading E_2 state at $\delta\gamma/\gamma_0 = 0$ are shown on the left hand side, while those for the leading A state at $\delta\gamma/\gamma_0 = -0.025$ are on the right hand side. Parameters $\{\lambda_R, D_0, \varepsilon_F\} = \{6, 6, 9.6\}$ meV.

E_2 states. The highest E_2 states of Fig. 9 at $\delta\gamma/\gamma_0 \simeq -0.025$ exhibit the behavior

$$\begin{pmatrix} d_{k,\eta}^1 \\ d_{k,\eta}^2 \end{pmatrix} = \beta_1 \begin{pmatrix} (\mathcal{X}_{\eta k}; 0, 0, 0) \\ (\mathcal{Y}_{\eta k}; 0, 0, 0) \end{pmatrix} + \beta_2 \nabla_{T,\eta k}^- \begin{pmatrix} (g_{\eta k}^x; 0, 0, 0) \\ (g_{\eta k}^y; 0, 0, 0) \end{pmatrix} + \eta \begin{pmatrix} (0; \mathcal{X}_{\eta k}, -\mathcal{Y}_{\eta k}, 0) \\ (0; -\mathcal{Y}_{\eta k}, -\mathcal{X}_{\eta k}, 0) \end{pmatrix}, \quad (47)$$

with β_1, β_2 small dimensionless parameters; this expression implies that the singlet components of these E_2 states are a linear combination of $(\mathcal{X}_{\eta k}, \mathcal{Y}_{\eta k})$ and $\mathbf{g}_{\eta k}$; the explicit ratio depends on the strength of SOC. The in-plane triplet components of (47) are dominant, while the singlet components are admixed. The next set of E_2 states in Fig. 9 take the form, e.g.,

$$\begin{pmatrix} d_{k,\eta}^1 \\ d_{k,\eta}^2 \end{pmatrix} \simeq \begin{pmatrix} (\mathcal{X}_{\eta k}; 0, 0, 0) \\ (\mathcal{Y}_{\eta k}; 0, 0, 0) \end{pmatrix} + \beta_1 \eta \begin{pmatrix} (0; \mathcal{X}_{\eta k}, -\mathcal{Y}_{\eta k}, 0) \\ (0; -\mathcal{Y}_{\eta k}, -\mathcal{X}_{\eta k}, 0) \end{pmatrix} + \beta_2 \eta \nabla_{T,\eta k}^- \begin{pmatrix} (0; g_{\eta k}^x \mathcal{X}_{\eta k}, g_{\eta k}^y \mathcal{X}_{\eta k}, 0) \\ (0; g_{\eta k}^x \mathcal{Y}_{\eta k}, g_{\eta k}^y \mathcal{Y}_{\eta k}, 0) \end{pmatrix}. \quad (48)$$

In contrast to (47), the E_2 state in Eq. (48) can be understood as resulting from the rotationally nontrivial combination of the $(\mathcal{X}_{\eta k}, \mathcal{Y}_{\eta k})$ with the single component the nodeless A state of Fig. 6. In this case, the singlet components are dominant and the triplet components are admixed. With this insight, we comment that the triplet components of (48) with coefficient β_2 are deduced as being the rotationally trivial combination $[(\hat{e}_x, \hat{e}_y, 0) \cdot (\mathbf{g}_{\eta k}^x, \mathbf{g}_{\eta k}^y, 0)]$ —as seen in the triplet components of the A state of Fig. 6—multiplied by the vector $(\mathcal{X}_{\eta k}, \mathcal{Y}_{\eta k})^T$. In terms of our symmetry analysis in Sec. III, the states in Eqs. (47) and (48) should be thought of as two different superpositions of E_{2g} in Eq. (22) and E_{2u} in Eq. (17), leading to Eq. (23) with nontrivial M_k , see also Fig. 4(b).

E_1 states. Finally, there exists E_1 states, which are precisely those presented in (26). These are purely out-of-plane triplets

and do not mix with singlets or in-plane triplets if only Rashba SOC is present.

V. CONCLUSION AND OUTLOOK

Summary. We presented the continuum model for a TMD/TTLG/TMD heterostructure, subject to two distinct arrangements—(i) inversion symmetric and (ii) mirror symmetric, see top two panels in Fig. 1. This difference has significant implications for the form of the proximitised spin-orbit coupling (SOC); with (i) the SOC does not itself generate spin splitting, but instead splitting can be induced via, e.g., an inversion-symmetry-breaking displacement field (D_0). In contrast, in (ii) an Ising SOC generates spin splitting, already at $D_0 = 0$. These results are summarized in Fig. 1. The inversion symmetric setup, which hosts a displacement-field-tunable spin splitting was the focus of the rest of the analysis.

Our objective was to systematically understand how the superconductivity of TTLG, referred to as the parent superconducting state, evolves under applied D_0 and SOC, where we considered both Rashba and Ising SOC. We accounted for a range of possible candidate parent superconducting states, including spin-singlet, -triplet, and -SO(4) ordering, with either nodeless or nodal momentum dependence. We exclusively focused on intervalley pairing, as it is expected to be favored over intravalley pairing due to time-reversal symmetry and an additional protection against disorder [75]. To achieve this goal, we pursued a three-fold analysis. First, we applied a mean-field gap equation (detailed in Sec. II B) to numerically compute the superconducting order parameters (see Sec. IV A), allowing for arbitrary momentum dependence. We supplemented this with analytic arguments to understand salient features (Sec. IV C), and we also provided a detailed symmetry analysis (Sec. III), which has the advantage of being independent of the particular assumptions—most notably the form of interactions—entering the gap equation and the mean-field approximation itself. These three approaches

complement each other well and yield a consistent picture for the evolution of superconductivity in TTLG with D_0 -tunable SOC.

For dominant Rashba SOC (expected for θ_{TMD} in Fig. 1 close to 30°), the system is predicted to exhibit phase transitions as a function of D_0 between two different pairing states if and only if triplet pairing is dominant in the parent TTLG system; this could be used to probe the spin structure of the superconducting state in TTLG in future experiments, e.g., by measuring the evolution of the critical temperature as a function of D_0 and magnetic field in our geometry (i). We have studied the phase diagram in the vicinity of the transition point, which either exhibits a first order transition or an intermediate regime of microscopic coexistence, see Fig. 8.

Experimental feasibility. First, given that TMD/TTLG/TMD has already been fabricated, extending this to TMD/TTLG/TMD appears to be within reach. Next, we note that the twist angle between the TMD and graphene layers does not require as much experimental control as one needs for the TTLG part. The challenge with symmetrically twisted TTLG is achieving the alignment of the outer two graphene layers; given that one is interested in small twist angles $\theta \sim 1^\circ$ – 2° —and the subsequent formation of a moiré pattern—even small angular variations can be dramatic as they lead to a superlattice modulation of the moiré pattern, see, e.g., Ref. [23]. On the other hand, we assert that adding TMD outer layers is less sensitive to angular variations; the outer TMD layers are placed at large twist angles, around $\theta_{\text{TMD}} \sim 30^\circ$, and so are not forming a relevant moiré pattern and small variations thereby have negligible effect.

Outlook. Future theoretical studies may build upon the results obtained here to consider further implications of the pairing states. In particular, they may take the array of superconducting order parameters from this work and construct the gauge-invariant bilinears of the orders, known as *vestigial orders* [76]. These orders break only a subset of the symmetries and often only discrete symmetries, allowing them to persist at temperatures above the critical phase coherence temperature of the underlying or constituent superconducting order. This persistence can influence the electronic behavior of the system outside of the superconducting phase. Given the exotic structure of the superconducting order parameters found here, one may hope to find exotic vestigial orders with clear experimental signatures. Additionally, the topological nature of the superconducting order parameters has not been considered in this work and, therefore, remains an open problem. Related systems have demonstrated the existence of higher-order topological superconductivity [77–80], including for intervalley paired states [79,80].

A direct extension of the present analysis would be to employ the inversion symmetric TMD/TTLG/TMD heterostructure, combined with inversion breaking D_0 , to study the evolution of candidate particle-hole phases in this system. Also their interplay with superconductivity will likely give rise to very interesting and rich physics [11,25,26,81–86]. Therefore, it would be instructive to analyze how they coexist or compete with superconductivity.

The ultimate goal of this analysis is to provoke future experimental studies of this highly tunable van der Waals heterostructure, to systematically investigate the influence of

spin splitting of the electronic bands on correlated phases in general, and, in particular, to use our systematic results as a means of distinguishing between various candidate parent superconducting states.

ACKNOWLEDGMENTS

M.S.S. acknowledges funding from the European Union (ERC-2021-STG, Project No. 101040651—SuperCorr). Views and opinions expressed are however those of the authors only and do not necessarily reflect those of the European Union or the European Research Council.

APPENDIX A: BAND STRUCTURE: EXTRA DETAILS

TTLG band Hamiltonian. As presented in Sec. II A, the continuum Hamiltonian is separated into four parts, $h_{k,\eta} = h_{k,\eta}^{(g)} + h_{k,\eta}^{(t)} + h_{k,\eta}^{(D)} + h_{k,\eta}^{(\text{SOC})}$; the terms $h_{k,\eta}^{(D)}$ and $h_{k,\eta}^{(\text{SOC})}$, which we think of as a perturbation in this work, were described in the main text, and here we provide the explicit form of the TTLG subsystem, i.e., the $h_{k,\eta}^{(g)} + h_{k,\eta}^{(t)}$. First, the contribution from the individual graphene layers is captured by,

$$(h_{k,+}^{(g)})_{\rho,\ell,s,\mathbf{G};\rho',\ell',s',\mathbf{G}'} = \delta_{\ell,\ell'} \delta_{s,s'} \delta_{\mathbf{G},\mathbf{G}'} v_F (\boldsymbol{\rho}_{\theta_\ell})_{\rho,\rho'} (\mathbf{k} + \mathbf{G} - (-1)^\ell \mathbf{q}_1/2), \quad (\text{A1})$$

$$(h_{k,-}^{(g)})_{\rho,\ell,s,\mathbf{G};\rho',\ell',s',\mathbf{G}'} = (h_{-k,+}^{(g)})_{\rho,\ell,s,-\mathbf{G};\rho',\ell',s',-\mathbf{G}'}, \quad (\text{A2})$$

where \mathbf{q}_1 connects the K and K' points of the MBZ and $\boldsymbol{\rho}_\theta = e^{i\theta} \rho_z/2 \boldsymbol{\rho} e^{-i\theta} \rho_z/2$. Second, the tunneling between the layers is modeled as,

$$(h_{k,+}^{(t)})_{\rho,\ell,s,\mathbf{G};\rho',\ell',s',\mathbf{G}'} = \sqrt{2} \delta_{s,s'} \begin{pmatrix} 0 & (T_{\mathbf{G}-\mathbf{G}'}^{\rho,\rho'}) & 0 \\ (T_{\mathbf{G}'-\mathbf{G}}^{\rho',\rho})^* & 0 & 0 \\ 0 & 0 & 0 \end{pmatrix}_{\ell,\ell'}, \quad (\text{A3})$$

$$(h_{k,-}^{(t)})_{\rho,\ell,s,\mathbf{G};\rho',\ell',s',\mathbf{G}'} = (h_{-k,+}^{(t)})_{\rho,\ell,s,-\mathbf{G};\rho',\ell',s',-\mathbf{G}'}, \quad (\text{A3})$$

where

$$T_{\delta\mathbf{G}} = \sum_{j=-1,0,1} \delta_{\delta\mathbf{G}+A_j,0} \left[w_0 \rho_0 + w_1 \begin{pmatrix} 0 & \omega^j \\ \omega^{-j} & 0 \end{pmatrix} \right], \quad (\text{A4})$$

$$\omega = e^{i\frac{2\pi}{3}}, \quad A_0 = 0, \quad A_1 = \mathbf{G}_1, \quad A_2 = \mathbf{G}_1 + \mathbf{G}_2. \quad (\text{A5})$$

Here w_0 and w_1 parametrize the strength of, respectively, the sublattice diagonal and off-diagonal interlayer hopping strengths. All results presented here take $w_0 = 0.875w_1$ and $w_1 = 110$ meV.

Extra plots. To supplement the band structure plots presented in Fig. 1, which compared the band structures of the two distinct configurations, here Figs. 10 and 11 provide a more comprehensive comparison for a range of SOC and D_0 strengths.

APPENDIX B: SYMMETRIZING THE GAP EQUATION

The gap equation (11) is a non-Hermitian eigenvalue problem; the order parameters $d_{\mu,k}$ presented in the main text

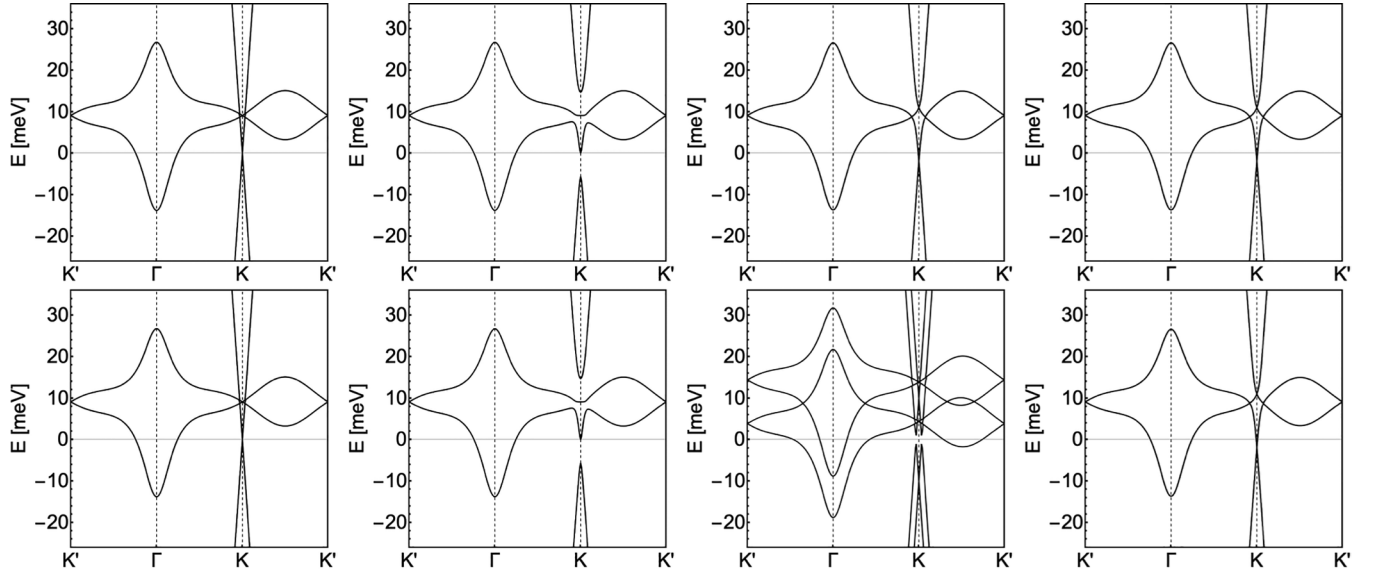


FIG. 10. Band structure at twist $\theta = 1.75^\circ$, with $\eta = 1$. Top row: $\theta_{\text{TMD}} + \pi$ (inversion symmetric stack). Bottom row: θ_{TMD} . The following combinations of SOC and D_0 : (i) $\lambda_R, \lambda_I, D_0 = \{0, 0, 0\}$ meV, (ii) $\lambda_R, \lambda_I, D_0 = \{10, 0, 0\}$ meV, (iii) $\lambda_R, \lambda_I, D_0 = \{0, 10, 0\}$ meV, (iv) and $\lambda_R, \lambda_I, D_0 = \{0, 0, 10\}$ meV.

are found by solving for the right eigenvector of the non-Hermitian matrix. However, since it is convenient to work with Hermitian matrices— especially for application of perturbation theory detailed in Appendix C— we here show how to symmetrize the gap equation (11). Assuming summation over repeated indices, the gap equation is written as

$$(\Gamma^{-1})_{k_1, k_2; \mu\nu} d_{\mu, k_2} = W_{k_1; \mu\nu} d_{\nu, k_1}. \quad (\text{B1})$$

In matrix notation, we perform the following steps to cast it into Hermitian form

$$\begin{aligned} (\Gamma^{-1})\bar{d} &= W\bar{d}, \\ U\Lambda U^\dagger \bar{d} &= W\bar{d}, \\ \Lambda \bar{f} &= U^\dagger W U \bar{f}, \\ \bar{h} &= \Lambda^{-\frac{1}{2}} U^\dagger W U \Lambda^{-\frac{1}{2}} \bar{h}. \end{aligned} \quad (\text{B2})$$

Since $\Gamma_{k_1, k_2; \mu\nu}$ is spin-diagonal in our modelling, then so too are U and $\Lambda^{-\frac{1}{2}}$. Moreover, Λ and $\Lambda^{-\frac{1}{2}}$ are completely diagonal, while $U = (U_{k, \chi_i}^{\mu\mu})$ contains, as column vectors, the orthonormal basis of spatial harmonics of Γ , which we index by χ_i . Using indices,

$$h_{\chi_i}^\mu = (\Lambda^{-\frac{1}{2}})_{\chi_i, \chi_i}^{\mu\mu} (U_{\chi_i, k_1}^\dagger)^{\mu\mu} W_{k_1}^{\mu\nu} U_{k_1, \chi_j}^{\nu\nu} (\Lambda^{-\frac{1}{2}})_{\chi_j, \chi_j}^{\nu\nu} h_{\chi_j}^\nu. \quad (\text{B3})$$

We solve for $h_{\chi_i}^\mu$ as eigenvectors and subsequently obtain the order parameter components $d_{\mu, k}$ via the inverse transformation

$$d_{\mu, k} = U_{k, \chi_j}^{\mu\nu} (\Lambda^{-\frac{1}{2}})_{\chi_j, \chi_j}^{\nu\nu} h_{\chi_j}^\nu. \quad (\text{B4})$$

It is these $d_{\mu, k}$ that are presented in the main text.

Finally, we model the momentum-dependent factor F_{k_1, k_2} , appearing in the potential (9), as Lorentzian-shaped about the two partially filled bands $\varepsilon_{+, n, k}$, with $n = 1, 2$, and with

an exponential factor favoring small angle scattering, i.e., $k_1 \simeq k_2$,

$$F_{k_1, k_2} = (1 + a_0 e^{-a_1 |k_1 - k_2|}) L_{k_1, \varepsilon_F} L_{k_2, \varepsilon_F}, \quad (\text{B5})$$

$$L_{k, \varepsilon_F} = \frac{1}{1 + a_2 [(\varepsilon_{+, 1, k} - \varepsilon_F)(\varepsilon_{+, 2, k} - \varepsilon_F)]^2 / \varepsilon_F^4}. \quad (\text{B6})$$

The parameters $\{a_0, a_1, a_2\} = \{3, 30, 9000\}10^3$ are chosen to demonstrate the momentum-dependent admixture of order parameters. We work in units where the monolayer graphene lattice constant $a = 1$.

APPENDIX C: PERTURBATIVE TREATMENT OF THE GAP EQUATION

Section IV C presented the key characteristics of the superconducting order parameters $d_{\mu, k}$, based on a perturbative treatment; in this Appendix we present the details of the perturbation expansion. For ease we reprint the gap equation (37) of the complementary model of Sec. IV C,

$$\begin{aligned} d_{0, k} &= \sum_k \Gamma_{k, k}^0 [\nabla_{T, k}^+ d_{0, k'} + \nabla_{T, k}^- \hat{\mathbf{g}}_k \cdot \mathbf{d}_{k'}], \\ \mathbf{d}_k &= \sum_k \Gamma_{k, k}^0 [\nabla_{T, k}^+ \mathbf{d}_{k'} + \nabla_{T, k}^- \hat{\mathbf{g}}_k d_{0, k'} \\ &\quad + 2 \nabla_{T, k}^0 [\hat{\mathbf{g}}_k (\hat{\mathbf{g}}_{k'} \cdot \mathbf{d}_{k'}) - \mathbf{d}_{k'}]]. \end{aligned} \quad (\text{C1})$$

We will treat terms $\propto \nabla_{T, k}^-$ as perturbations and note that these terms are responsible for mixing singlet and triplet components. In more compact notation, this is rewritten as

$$\bar{d} = \Gamma W \bar{d}. \quad (\text{C2})$$

Our perturbation theory begins by splitting the matrix $W = W^0 + W^1$, where $W^0 \propto \delta_{\mu\nu}$ and the perturbation $(W^1)^{\mu\nu}$ is off-diagonal in spin; it contains SOC, via the $g_{k, \mu}$ -vectors as well as factors of ∇_k^- , which are the difference

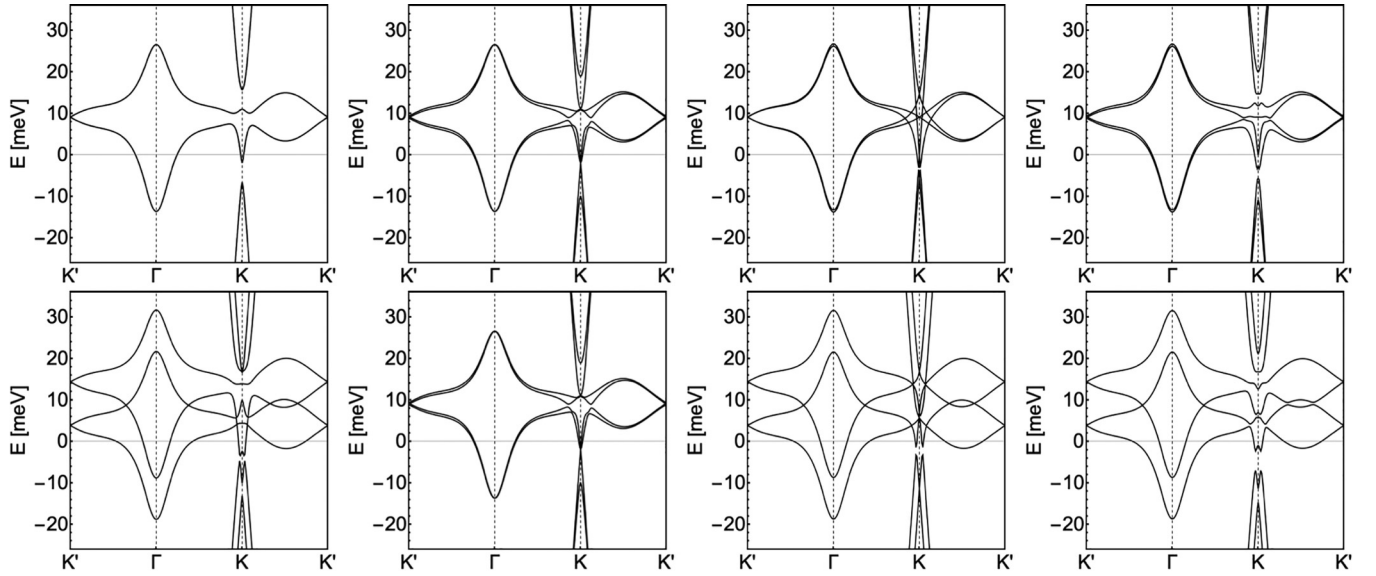


FIG. 11. Band structure at twist $\theta = 1.75^\circ$, with $\eta = 1$. Top row: $\theta_{\text{TMD}} + \pi$ (inversion symmetric stack). Bottom row: θ_{TMD} . The following combinations of SOC and D_0 : (i) $\lambda_R, \lambda_I, D_0 = \{10, 10, 0\}$ meV, (vi) $\lambda_R, \lambda_I, D_0 = \{10, 0, 10\}$ meV, (vii) $\lambda_R, \lambda_I, D_0 = \{0, 10, 10\}$ meV, and (viii) $\lambda_R, \lambda_I, D_0 = \{10, 10, 10\}$ meV.

of thermal occupation factors of the spin split bands and which changes sign in between the corresponding Fermi surfaces.

A state with admixed triplet. Consider a zeroth-order, spin-singlet ($\mu = 0$) eigenstate, which necessarily belongs to the trivial spatial irrep $\chi_i \in A$. We denote this zeroth-order state as

$$\bar{h}^A = (h_{0,\chi_i}^A, \mathbf{0}), \quad (\text{C3})$$

which is written as a four-vector in spin, and with the singlet component, h_{0,χ_i}^A , indexed by the harmonics χ_i . The corresponding eigenvalue is denoted E_A . Hence we use the label A to denote the linear combination of all $\chi_i \in A$, which would be found via direct diagonalisation of (B3) with $W \rightarrow W^0$. Next, we denote a generic eigenstate \bar{h}^R in a *spatial* irrep R and with corresponding eigenvalue E_R . Note (i) there can be multiple orthogonal eigenstates belonging to the same irrep R and (ii) the combination of spin and space may have a different combined spin-spatial irrep, but for the presentation here, it is convenient to talk about pure spatial irreps.

Now we consider the perturbation W^1 and determine the first-order correction to \bar{h}^A , i.e., find the \bar{h}^R which become admixed via the perturbation. This is done via standard quantum mechanical perturbation theory,

$$\tilde{\bar{h}}^A = \bar{h}^A + \sum_R \frac{1}{E_A - E_R} [(\bar{h}^R)^\dagger \Lambda^{-\frac{1}{2}} U^\dagger W^1 U \Lambda^{-\frac{1}{2}} \bar{h}^A] \bar{h}^R, \quad (\text{C4})$$

whereby the perturbing potential is $\Lambda^{-\frac{1}{2}} U^\dagger W^1 U \Lambda^{-\frac{1}{2}}$. Next, we can greatly simplify the expression by returning to the original \bar{d} variables; the transformation is $\bar{d}_R = U \Lambda^{-\frac{1}{2}} \bar{h}_R$, and here the \bar{d}_R are vectors in the spatial irrep R . Applying this transformation to the perturbed-eigenvector

expression (C4),

$$U \Lambda^{-\frac{1}{2}} \tilde{\bar{h}}^A = U \Lambda^{-\frac{1}{2}} \bar{h}_A^0 + \sum_R \frac{1}{E_A - E_R} \times [\bar{h}_R^\dagger \Lambda^{-\frac{1}{2}} U^\dagger W^1 U \Lambda^{-\frac{1}{2}} \bar{h}_A] U \Lambda^{-\frac{1}{2}} \bar{h}_R, \quad (\text{C5})$$

we obtain

$$\tilde{\bar{d}}_A = \bar{d}_A + \sum_R \frac{1}{E_A - E_R} [\bar{d}_R^\dagger W^1 \bar{d}_A] \bar{d}_R. \quad (\text{C6})$$

Reinstating indices and the explicit form of W^1 , which follows from the gap equation (C1), we arrive at

$$\begin{aligned} \tilde{d}_{\mu,k}^A &= d_{0,k}^A \delta_{\mu,0} + \sum_{R,k_1} \frac{1}{E_A - E_R} [(d_{\mu,k_1}^R)^\dagger (W_{k_1}^1)^{\mu 0} d_{0,k_1}^A] d_{\mu,k}^R \\ &= d_{0,k}^A \delta_{\mu,0} + \sum_{R,k_1} \frac{1}{E_A - E_R} [(d_{\mu,k_1}^R)^\dagger \nabla_{k_1}^- \mathbf{g}_{k_1}^\mu d_{0,k_1}^A] d_{\mu,k}^R. \end{aligned} \quad (\text{C7})$$

The expression (C10) represents the explicit result of our perturbation theory, without any approximations. Now, based on (C10), we introduce an approximate expression. First, examining the matrix element, $\sum_{k_1} [(d_{\mu,k_1}^R)^\dagger \nabla_{k_1}^- \mathbf{g}_{k_1}^\mu d_{0,k_1}^A]$, we see that it is nonzero only for those d_{μ,k_1}^R that transform in the same irrep as $\nabla_{k_1}^- \mathbf{g}_{k_1}^\mu d_{0,k_1}^A$. Since $\nabla_{k_1}^-$ changes sign radially between the two spin split Fermi surfaces, while the $\mathbf{g}_{k_1}^\mu$ change sign upon winding about the Fermi surfaces, then only those d_{μ,k_1}^R that exhibit both the radial and angular sign changes will have an appreciable overlap. Therefore, maximal overlap occurs for $d_{\mu,k;\text{projected}}^R \simeq \nabla_{k_1}^- \mathbf{g}_{k_1}^\mu d_{0,k_1}^A$, and we arrive at

the approximation

$$\tilde{d}_{k,A}^\mu \simeq d_{0,k}^A \delta_{\mu,0} + \beta \nabla_k^- \mathbf{g}_{k_1}^\mu d_{k,A}^0, \quad (\text{C8})$$

with numerical factors absorbed into the constant β . Upon reinstating the η index and employing compact vector notation, the perturbed singlet A state becomes

$$\tilde{d}_{k,\eta}^A = (d_{0,\eta,k}^A; \beta \eta \nabla_{T,\eta,k}^- \hat{\mathbf{g}}_{\eta,k} d_{0,\eta,k}^A), \quad (\text{C9})$$

Noting that ∇_k^- changes sign between the fermi surfaces, while the $\mathbf{g}_{k_1}^\mu$ winds about the fermi surface, together this gives a Möbius-like spin-triplet texture to the admixed state, cf. Ref. [59].

Comment. It appears that from (C6), the form of the potential Γ does not show up and hence the admixture is set purely by the perturbation W^1 . First, we can only arrive at (C6) if Γ is invertible and positive definite. Second, it is the \hat{h} eigenvectors of (B3) that are normalized, while the \vec{d} -vectors are found via the nonunitary transformation $\vec{d} = \Lambda^{-\frac{1}{2}} U \hat{h}$. Due to this nonunitary transformation, the potential Γ then influences the magnitude of the \vec{d} -vectors.

E state with admixed singlet. Focusing now on the in-plane triplet eigenstate, which at zeroth-order is denoted $d_{j,k}^E \in E$ IR, where index $j = 1$ and 2 enumerates the in-plane triplet components, and has corresponding eigenvalue E_E . A first-order perturbation in \hat{W}^1 admixes a singlet component into

this triplet,

$$\begin{aligned} \tilde{d}_{\mu,k}^E &= d_{\mu,k}^E (\delta_{\mu,1} + \delta_{\mu,2}) + \delta_{\mu,0} \sum_{R,k_1,j'} \frac{1}{E_E - E_R} \\ &\times [(d_{0,k_1}^R)^\dagger (W_{k_1}^1)^{0j'} d_{j',k_1}^E] d_{0,k}^R \end{aligned} \quad (\text{C10})$$

$$\begin{aligned} &= d_{\mu,k}^E (\delta_{\mu,1} + \delta_{\mu,2}) + \delta_{\mu,0} \sum_{R,k_1} \frac{1}{E_E - E_R} \\ &\times [(d_{0,k_1}^R)^\dagger \nabla_{k_1}^- \mathbf{g}_{k_1} \cdot \mathbf{d}_{k_1}^E] d_{0,k}^R. \end{aligned} \quad (\text{C11})$$

Noting that each component of $d_{j,k}^E$ transforms trivially under a pure spatial rotation, then the $d_{0,k}^R$ which poses a non-negligible overlap with $\nabla_k^- \mathbf{g}_k \cdot \mathbf{d}_k^E$ must exhibit both the radial and angular sign changes. Like our discussion above, this leads to the approximate expression,

$$\tilde{d}_{\mu,k}^E \simeq d_{\mu,k}^E (\delta_{\mu,1} + \delta_{\mu,2}) + \beta \nabla_k^- \mathbf{g}_k \cdot \mathbf{d}_k^E \delta_{\mu,0}. \quad (\text{C12})$$

Here β represents a numerical constant, different from (C8). Reinstating the valley index η , and conforming to the more compact notation of the main text, this becomes

$$\tilde{d}_k^E = (\beta \nabla_{\eta,k}^- \mathbf{g}_{\eta,k} \cdot \mathbf{d}_{\eta,k}^E; \eta \mathbf{d}_{\eta,k}^E). \quad (\text{C13})$$

This perturbative expression shows that the admixed singlet exhibits sign changes going around the Fermi surfaces, due to $\hat{\mathbf{g}}_{\eta,k} \cdot \mathbf{d}_{\eta,k}^E$, and changes sign between the two spin split Fermi surfaces, due to $\nabla_{T,\eta,k}^-$. Both such features are seen in the admixed singlet component $d_{0,k}$ obtained from the full numerical solution of the gap equation.

-
- [1] A. H. MacDonald, Bilayer Graphene's wicked, twisted road, *Physics* **12**, 12 (2019).
- [2] E. Y. Andrei and A. H. MacDonald, Graphene bilayers with a twist, *Nat. Mater.* **19**, 1265 (2020).
- [3] Y. Cao, V. Fatemi, A. Demir, S. Fang, S. L. Tomarken, J. Y. Luo, J. D. Sanchez-Yamagishi, K. Watanabe, T. Taniguchi, E. Kaxiras, R. C. Ashoori, and P. Jarillo-Herrero, Correlated insulator behaviour at half-filling in magic-angle graphene superlattices, *Nature (London)* **556**, 80 (2018).
- [4] Y. Cao, V. Fatemi, S. Fang, K. Watanabe, T. Taniguchi, E. Kaxiras, and P. Jarillo-Herrero, Unconventional superconductivity in magic-angle graphene superlattices, *Nature (London)* **556**, 43 (2018).
- [5] M. Yankowitz, S. Chen, H. Polshyn, Y. Zhang, K. Watanabe, T. Taniguchi, D. Graf, A. F. Young, and C. R. Dean, Tuning superconductivity in twisted bilayer graphene, *Science* **363**, 1059 (2019).
- [6] X. Lu, P. Stepanov, W. Yang, M. Xie, M. A. Aamir, I. Das, C. Urgell, K. Watanabe, T. Taniguchi, G. Zhang, A. Bachtold, A. H. MacDonald, and D. K. Efetov, Superconductors, orbital magnets and correlated states in magic-angle bilayer graphene, *Nature (London)* **574**, 653 (2019).
- [7] Y. Choi, J. Kemmer, Y. Peng, A. Thomson, H. Arora, R. Polski, Y. Zhang, H. Ren, J. Alicea, G. Refael, F. von Oppen, K. Watanabe, T. Taniguchi, and S. Nadj-Perge, Electronic correlations in twisted bilayer graphene near the magic angle, *Nat. Phys.* **15**, 1174 (2019).
- [8] A. Kerelsky, L. J. McGilly, D. M. Kennes, L. Xian, M. Yankowitz, S. Chen, K. Watanabe, T. Taniguchi, J. Hone, C. Dean, A. Rubio, and A. N. Pasupathy, Maximized electron interactions at the magic angle in twisted bilayer graphene, *Nature (London)* **572**, 95 (2019).
- [9] Y. Xie, B. Lian, B. Jäck, X. Liu, C.-L. Chiu, K. Watanabe, T. Taniguchi, B. A. Bernevig, and A. Yazdani, Spectroscopic signatures of many-body correlations in magic-angle twisted bilayer graphene, *Nature (London)* **572**, 101 (2019).
- [10] Y. Jiang, X. Lai, K. Watanabe, T. Taniguchi, K. Haule, J. Mao, and E. Y. Andrei, Charge order and broken rotational symmetry in magic-angle twisted bilayer graphene, *Nature (London)* **573**, 91 (2019).
- [11] A. L. Sharpe, E. J. Fox, A. W. Barnard, J. Finney, K. Watanabe, T. Taniguchi, M. A. Kastner, and D. Goldhaber-Gordon, Emergent ferromagnetism near three-quarters filling in twisted bilayer graphene, *Science* **365**, 605 (2019).
- [12] M. Serlin, C. L. Tschirhart, H. Polshyn, Y. Zhang, J. Zhu, K. Watanabe, T. Taniguchi, L. Balents, and A. F. Young, Intrinsic quantized anomalous hall effect in a moiré heterostructure, *Science* **367**, 900 (2020).
- [13] Y. Cao, D. Rodan-Legrain, J. M. Park, N. F. Q. Yuan, K. Watanabe, T. Taniguchi, R. M. Fernandes, L. Fu, and P. Jarillo-Herrero, Nematicity and competing orders in superconducting magic-angle graphene, *Science* **372**, 264 (2021).
- [14] Y. Xie, A. T. Pierce, J. M. Park, D. E. Parker, E. Khalaf, P. Ledwith, Y. Cao, S. H. Lee, S. Chen, P. R. Forrester,

- K. Watanabe, T. Taniguchi, A. Vishwanath, P. Jarillo-Herrero, and A. Yacoby, Fractional chern insulators in magic-angle twisted bilayer graphene, *Nature (London)* **600**, 439 (2021).
- [15] C. Rubio-Verdú, S. Turkel, Y. Song, L. Klebl, R. Samajdar, M. S. Scheurer, J. W. F. Venderbos, K. Watanabe, T. Taniguchi, H. Ochoa, L. Xian, D. M. Kennes, R. M. Fernandes, Á. Rubio, and A. N. Pasupathy, Moirénematic phase in twisted double bilayer graphene, *Nat. Phys.* **18**, 196 (2022).
- [16] H. S. Arora, R. Polski, Y. Zhang, A. Thomson, Y. Choi, H. Kim, Z. Lin, I. Z. Wilson, X. Xu, J.-H. Chu, K. Watanabe, T. Taniguchi, J. Alicea, and S. Nadj-Perge, Superconductivity in metallic twisted bilayer graphene stabilized by WSe₂, *Nature (London)* **583**, 379 (2020).
- [17] Y. Choi, H. Kim, Y. Peng, A. Thomson, C. Lewandowski, R. Polski, Y. Zhang, H. S. Arora, K. Watanabe, T. Taniguchi, J. Alicea, and S. Nadj-Perge, Correlation-driven topological phases in magic-angle twisted bilayer graphene, *Nature (London)* **589**, 536 (2021).
- [18] J.-X. Lin, Y.-H. Zhang, E. Morissette, Z. Wang, S. Liu, D. Rhodes, K. Watanabe, T. Taniguchi, J. Hone, and J. I. A. Li, Spin-orbit driven ferromagnetism at half moire filling in magic-angle twisted bilayer graphene, *Science* **375**, 437 (2022).
- [19] J. M. Park, Y. Cao, K. Watanabe, T. Taniguchi, and P. Jarillo-Herrero, Tunable strongly coupled superconductivity in magic-angle twisted trilayer graphene, *Nature (London)* **590**, 249 (2021).
- [20] Z. Hao, A. M. Zimmerman, P. Ledwith, E. Khalaf, D. H. Najafabadi, K. Watanabe, T. Taniguchi, A. Vishwanath, and P. Kim, Electric field-tunable superconductivity in alternating-twist magic-angle trilayer graphene, *Science* **371**, 1133 (2021).
- [21] Y. Cao, J. M. Park, K. Watanabe, T. Taniguchi, and P. Jarillo-Herrero, Pauli-limit violation and re-entrant superconductivity in moirégraphene, *Nature (London)* **595**, 526 (2021).
- [22] H. Kim, Y. Choi, C. Lewandowski, A. Thomson, Y. Zhang, R. Polski, K. Watanabe, T. Taniguchi, J. Alicea, and S. Nadj-Perge, Spectroscopic signatures of strong correlations and unconventional superconductivity in twisted trilayer graphene, *arXiv:2109.12127*.
- [23] S. Turkel, J. Swann, Z. Zhu, M. Christos, K. Watanabe, T. Taniguchi, S. Sachdev, M. S. Scheurer, E. Kaxiras, C. R. Dean, and A. N. Pasupathy, Orderly disorder in magic-angle twisted trilayer graphene, *Science* **376**, 193 (2022).
- [24] X. Liu, N. J. Zhang, K. Watanabe, T. Taniguchi, and J. I. A. Li, Isospin order in superconducting magic-angle twisted trilayer graphene, *Nat. Phys.* **18**, 522 (2022).
- [25] P. Siriviboon, J.-X. Lin, X. Liu, H. D. Scammell, S. Liu, D. Rhodes, K. Watanabe, T. Taniguchi, J. Hone, M. S. Scheurer, and J. I. A. Li, A new flavor of correlation and superconductivity in small twist-angle trilayer graphene, *arXiv:2112.07127*.
- [26] J.-X. Lin, P. Siriviboon, H. D. Scammell, S. Liu, D. Rhodes, K. Watanabe, T. Taniguchi, J. Hone, M. S. Scheurer, and J. I. A. Li, Zero-field superconducting diode effect in small-twist-angle trilayer graphene, *Nat. Phys.* **18**, 1221 (2022).
- [27] J. Díez-Mérida, A. Díez-Carlón, S. Y. Yang, Y.-M. Xie, X.-J. Gao, J. Senior, K. Watanabe, T. Taniguchi, X. Lu, A. P. Higginbotham, K. T. Law, and D. K. Efetov, Symmetry-broken josephson junctions and superconducting diodes in magic-angle twisted bilayer graphene, *Nat. Commun.* **14**, 2396 (2023).
- [28] J. A. Sobral, S. Obernauer, S. Turkel, A. N. Pasupathy, and M. S. Scheurer, Machine learning microscopic form of nematic order in twisted double-bilayer graphene, *Nat. Commun.* **14**, 5012 (2023).
- [29] A. Jaoui, I. Das, G. Di Battista, J. Díez-Mérida, X. Lu, K. Watanabe, T. Taniguchi, H. Ishizuka, L. Levitov, and D. K. Efetov, Quantum critical behaviour in magic-angle twisted bilayer graphene, *Nat. Phys.* **18**, 633 (2022).
- [30] E. Morissette, J.-X. Lin, D. Sun, L. Zhang, S. Liu, D. Rhodes, K. Watanabe, T. Taniguchi, J. Hone, J. Pollanen, M. S. Scheurer, M. Lilly, A. Mounce, and J. I. A. Li, Dirac revivals drive a resonance response in twisted bilayer graphene, *Nat. Phys.* **19**, 1156 (2023).
- [31] H. Min, J. E. Hill, N. A. Sinitsyn, B. R. Sahu, L. Kleinman, and A. H. MacDonald, Intrinsic and rashba spin-orbit interactions in graphene sheets, *Phys. Rev. B* **74**, 165310 (2006).
- [32] D. Huertas-Hernando, F. Guinea, and A. Brataas, Spin-orbit coupling in curved graphene, fullerenes, nanotubes, and nanotube caps, *Phys. Rev. B* **74**, 155426 (2006).
- [33] M. Z. Hasan and C. L. Kane, Colloquium: Topological insulators, *Rev. Mod. Phys.* **82**, 3045 (2010).
- [34] T. Wang, N. Bultinck, and M. P. Zaletel, Flat-band topology of magic angle graphene on a transition metal dichalcogenide, *Phys. Rev. B* **102**, 235146 (2020).
- [35] J. Kang and O. Vafek, Strong coupling phases of partially filled twisted bilayer graphene narrow bands, *Phys. Rev. Lett.* **122**, 246401 (2019).
- [36] K. Seo, V. N. Kotov, and B. Uchoa, Ferromagnetic mott state in twisted graphene bilayers at the magic angle, *Phys. Rev. Lett.* **122**, 246402 (2019).
- [37] M. Xie and A. H. MacDonald, Nature of the correlated insulator states in twisted bilayer graphene, *Phys. Rev. Lett.* **124**, 097601 (2020).
- [38] N. Bultinck, E. Khalaf, S. Liu, S. Chatterjee, A. Vishwanath, and M. P. Zaletel, Ground state and hidden symmetry of magic-angle graphene at even integer filling, *Phys. Rev. X* **10**, 031034 (2020).
- [39] B. Lian, Z.-D. Song, N. Regnault, D. K. Efetov, A. Yazdani, and B. A. Bernevig, Twisted bilayer graphene. iv. exact insulator ground states and phase diagram, *Phys. Rev. B* **103**, 205414 (2021).
- [40] M. Christos, S. Sachdev, and M. S. Scheurer, Correlated insulators, semimetals, and superconductivity in twisted trilayer graphene, *Phys. Rev. X* **12**, 021018 (2022).
- [41] P. H. Wilhelm, T. C. Lang, M. S. Scheurer, and A. M. Läuchli, Non-coplanar magnetism, topological density wave order and emergent symmetry at half-integer filling of moiré Chern bands, *SciPost Phys.* **14**, 040 (2023).
- [42] H. D. Scammell, J. I. A. Li, and M. S. Scheurer, Theory of zero-field superconducting diode effect in twisted trilayer graphene, *2D Mater.* **9**, 025027 (2022).
- [43] J. F. Sierra, J. Fabian, R. K. Kawakami, S. Roche, and S. O. Valenzuela, Van der waals heterostructures for spintronics and opto-spintronics, *Nat. Nanotechnol.* **16**, 856 (2021).
- [44] M. Liu, L. Wang, and G. Yu, Developing graphene-based moiré heterostructures for twistrionics, *Adv. Sci.* **9**, 2103170 (2022).
- [45] A. Veneri, D. T. S. Perkins, C. G. Péterfalvi, and A. Ferreira, Twist angle controlled collinear edelstein effect in van der waals heterostructures, *Phys. Rev. B* **106**, L081406 (2022).
- [46] A. Avsar, J. Y. Tan, T. Taychatanapat, J. Balakrishnan, G. K. W. Koon, Y. Yeo, J. Lahiri, A. Carvalho, A. S. Rodin, E. C. T.

- O'Farrell, G. Eda, A. H. Castro Neto, and B. Özyilmaz, Spin-orbit proximity effect in graphene, *Nat. Commun.* **5**, 4875 (2014).
- [47] Z. Wang, D.-K. Ki, H. Chen, H. Berger, A. H. MacDonald, and A. F. Morpurgo, Strong interface-induced spin-orbit interaction in graphene on WS₂, *Nat. Commun.* **6**, 8339 (2015).
- [48] Z. Wang, D.-K. Ki, J. Y. Khoo, D. Mauro, H. Berger, L. S. Levitov, and A. F. Morpurgo, Origin and magnitude of 'designer' spin-orbit interaction in graphene on semiconducting transition metal dichalcogenides, *Phys. Rev. X* **6**, 041020 (2016).
- [49] M. Gmitra and J. Fabian, Graphene on transition-metal dichalcogenides: A platform for proximity spin-orbit physics and optospintronics, *Phys. Rev. B* **92**, 155403 (2015).
- [50] Y. Li and M. Koshino, Twist-angle dependence of the proximity spin-orbit coupling in graphene on transition-metal dichalcogenides, *Phys. Rev. B* **99**, 075438 (2019).
- [51] A. David, P. Rakyta, A. Kormányos, and G. Burkard, Induced spin-orbit coupling in twisted graphene-transition metal dichalcogenide heterobilayers: Twistronics meets spintronics, *Phys. Rev. B* **100**, 085412 (2019).
- [52] T. Naimier, K. Zollner, M. Gmitra, and J. Fabian, Twist-angle dependent proximity induced spin-orbit coupling in graphene/transition metal dichalcogenide heterostructures, *Phys. Rev. B* **104**, 195156 (2021).
- [53] S. Lee, D. J. P. de Sousa, Y.-K. Kwon, F. de Juan, Z. Chi, F. Casanova, and T. Low, Charge-to-spin conversion in twisted graphene/WSe₂ heterostructures, *Phys. Rev. B* **106**, 165420 (2022).
- [54] C. G. Péterfalvi, A. David, P. Rakyta, G. Burkard, and A. Kormányos, Quantum interference tuning of spin-orbit coupling in twisted van der waals trilayers, *Phys. Rev. Res.* **4**, L022049 (2022).
- [55] J. O. Island, X. Cui, C. Lewandowski, J. Y. Khoo, E. M. Spanton, H. Zhou, D. Rhodes, J. C. Hone, T. Taniguchi, K. Watanabe, L. S. Levitov, M. P. Zaletel, and A. F. Young, Spin-orbit-driven band inversion in bilayer graphene by the van der waals proximity effect, *Nature (London)* **571**, 85 (2019).
- [56] M. P. Zaletel and J. Y. Khoo, The gate-tunable strong and fragile topology of multilayer-graphene on a transition metal dichalcogenide, *arXiv:1901.01294*.
- [57] K. Zollner and J. Fabian, Bilayer graphene encapsulated within monolayers of WS₂ or Cr₂Ge₂Te₆: Tunable proximity spin-orbit or exchange coupling, *Phys. Rev. B* **104**, 075126 (2021).
- [58] K. Zollner, M. Gmitra, and J. Fabian, Proximity spin-orbit and exchange coupling in ABA and ABC trilayer graphene van der waals heterostructures, *Phys. Rev. B* **105**, 115126 (2022).
- [59] H. D. Scammell and M. S. Scheurer, Tunable superconductivity and möbius fermi surfaces in an inversion-symmetric twisted van der waals heterostructure, *Phys. Rev. Lett.* **130**, 066001 (2023).
- [60] M. Oh, K. P. Nuckolls, D. Wong, R. L. Lee, X. Liu, K. Watanabe, T. Taniguchi, and A. Yazdani, Evidence for unconventional superconductivity in twisted bilayer graphene, *Nature (London)* **600**, 240 (2021).
- [61] H. Kim, Y. Choi, C. Lewandowski, A. Thomson, Y. Zhang, R. Polski, K. Watanabe, T. Taniguchi, J. Alicea, and S. Nadj-Perge, Spectroscopic signatures of strong correlations and unconventional superconductivity in twisted trilayer graphene, *arXiv:2109.12127*.
- [62] J. M. B. Lopes dos Santos, N. M. R. Peres, and A. H. Castro Neto, Graphene bilayer with a twist: electronic structure, *Phys. Rev. Lett.* **99**, 256802 (2007).
- [63] R. Bistritzer and A. H. MacDonald, Moiré bands in twisted double-layer graphene, *Proc. Natl. Acad. Sci. USA* **108**, 12233 (2011).
- [64] J. M. B. Lopes dos Santos, N. M. R. Peres, and A. H. Castro Neto, Continuum model of the twisted graphene bilayer, *Phys. Rev. B* **86**, 155449 (2012).
- [65] E. Khalaf, A. J. Kruchkov, G. Tarnopolsky, and A. Vishwanath, Magic angle hierarchy in twisted graphene multilayers, *Phys. Rev. B* **100**, 085109 (2019).
- [66] X. Li, F. Wu, and A. H. MacDonald, Electronic structure of single-twist trilayer graphene, *arXiv:1907.12338*.
- [67] D. Călugăru, F. Xie, Z.-D. Song, B. Lian, N. Regnault, and B. A. Bernevig, Twisted symmetric trilayer graphene: Single-particle and many-body hamiltonians and hidden nonlocal symmetries of trilayer moiré systems with and without displacement field, *Phys. Rev. B* **103**, 195411 (2021).
- [68] C. Xu and L. Balents, Topological superconductivity in twisted multilayer graphene, *Phys. Rev. Lett.* **121**, 087001 (2018).
- [69] Y.-Z. You and A. Vishwanath, Superconductivity from valley fluctuations and approximate SO(4) symmetry in a weak coupling theory of twisted bilayer graphene, *npj Quantum Mater.* **4**, 16 (2019).
- [70] M. S. Scheurer and R. Samajdar, Pairing in graphene-based moiré superlattices, *Phys. Rev. Res.* **2**, 033062 (2020).
- [71] E. Lake, A. S. Patri, and T. Senthil, Pairing symmetry of twisted bilayer graphene: A phenomenological synthesis, *Phys. Rev. B* **106**, 104506 (2022).
- [72] R. M. Fernandes and A. J. Millis, Nematicity as a probe of superconducting pairing in iron-based superconductors, *Phys. Rev. Lett.* **111**, 127001 (2013).
- [73] V. Kozii, H. Isobe, J. W. F. Venderbos, and L. Fu, Nematic superconductivity stabilized by density wave fluctuations: Possible application to twisted bilayer graphene, *Phys. Rev. B* **99**, 144507 (2019).
- [74] M. Hoyer, S. V. Syzranov, and J. Schmalian, Effect of weak disorder on the phase competition in iron pnictides, *Phys. Rev. B* **89**, 214504 (2014).
- [75] R. Samajdar and M. S. Scheurer, Microscopic pairing mechanism, order parameter, and disorder sensitivity in moiré superlattices: Applications to twisted double-bilayer graphene, *Phys. Rev. B* **102**, 064501 (2020).
- [76] R. M. Fernandes, P. P. Orth, and J. Schmalian, Intertwined vestigial order in quantum materials: Nematicity and beyond, *Annu. Rev. Condens. Matter Phys.* **10**, 133 (2019).
- [77] T. Li, J. Ingham, and H. D. Scammell, Artificial graphene: Unconventional superconductivity in a honeycomb superlattice, *Phys. Rev. Res.* **2**, 043155 (2020).
- [78] A. Chew, Y. Wang, B. A. Bernevig, and Z.-D. Song, Higher-order topological superconductivity in twisted bilayer graphene, *Phys. Rev. B* **107**, 094512 (2023).
- [79] T. Li, M. Geier, J. Ingham, and H. Scammell, Higher-order topological superconductivity from repulsive interactions in kagome and honeycomb systems, *2D Mater.* **9**, 015031 (2022).
- [80] H. D. Scammell, J. Ingham, M. Geier, and T. Li, Intrinsic first- and higher-order topological superconductivity in a doped topological insulator, *Phys. Rev. B* **105**, 195149 (2022).

- [81] J. Liu and X. Dai, Orbital magnetic states in moiré graphene systems, *Nat. Rev. Phys.* **3**, 367 (2021).
- [82] P. P. Poduval and M. S. Scheurer, Vestigial singlet pairing in a fluctuating magnetic triplet superconductor: Applications to graphene moiré systems, [arXiv:2301.01344](https://arxiv.org/abs/2301.01344).
- [83] V. Kozii, M. P. Zaletel, and N. Bultinck, Spin-triplet superconductivity from intervalley goldstone modes in magic-angle graphene, *Phys. Rev. B* **106**, 235157 (2022).
- [84] M. Christos, S. Sachdev, and M. S. Scheurer, Nodal band-off-diagonal superconductivity in twisted graphene superlattices, *Nat. Commun.* **14**, 7134 (2023).
- [85] N. Parthenios and L. Classen, Twisted bilayer graphene at charge neutrality: competing orders of SU(4) Dirac fermions, *Phys. Rev. B* **108**, 235120 (2023).
- [86] J. Ingham, T. Li, M. S. Scheurer, and H. D. Scammell, Quadratic dirac fermions and the competition of ordered states in twisted bilayer graphene, [arXiv:2308.00748](https://arxiv.org/abs/2308.00748).